

# A one-stage high-order gas-kinetic scheme for multi-component flows with interface-sharpening technique

Shiyi Li<sup>a</sup>, Dongmi Luo<sup>a</sup>, Jianxian Qiu<sup>b</sup>, Song Jiang<sup>a</sup>, Yibing Chen<sup>a,\*</sup>

<sup>a</sup> Institute of Applied Physics and Computational Mathematics, Beijing 100191, China

<sup>b</sup> School of Mathematical Sciences and Fujian Provincial Key Laboratory of Mathematical Modeling and High-Performance Scientific Computation, Xiamen University, Xiamen, Fujian 361005, China

## ARTICLE INFO

### Article history:

Received 29 November 2022

Received in revised form 27 May 2023

Accepted 19 June 2023

Available online 22 June 2023

### Keywords:

Gas-kinetic scheme

Multi-component flow

One-stage method

High-order accuracy

Interface-sharpening technique

## ABSTRACT

We propose a one-stage high-order gas-kinetic scheme (GKS) with interface-sharpening technique for the 4-equations model of compressible multi-component stiffened-gas flows. The scheme is constructed based on the framework of a one-stage efficient high-order GKS (EHGKS), which can achieve uniform high-order accuracy in both space and time. The main idea in the construction of the new scheme consists of three parts. Firstly, different from the original EHGKS, the non-oscillatory kinetic (NOK) flux is introduced to compute the leading term and the related flux evaluations, which enables the modified EHGKS suitable for stiffened gases, together with no pressure and velocity oscillations across the contact discontinuities. Then the modified scheme is utilized to discretize the conservative parts of the 4-equations model. Secondly, in order to avoid the oscillations across material interfaces, a high-order GKS is derived to solve the non-conservative parts of the 4-equations model following the idea of Abgrall [1]. Finally, to further reduce the over diffusion near a material interface, a simple interface-sharpening technique is developed, which combines the idea of interface construction and downwind scheme. The numerical results demonstrate that the proposed scheme can not only achieve the designed uniform accuracy in both space and time, but also sharply capture material interfaces.

© 2023 Elsevier Inc. All rights reserved.

## 1. Introduction

In the past decades, numerical simulations for the compressible immiscible multi-component flows have attracted much attention. The diffuse interface method (DIM), which presents numerically diffused zones at a material interface, provides an efficient and robust framework [53,1,57] in this issue. Since the interface is considered as an artificial mixture zone, DIM is naturally suitable for large interface deformations and topological changes. However, particular attention must be paid since a DIM always introduces over diffusion near the material interface. Even worse, it will definitely fail to identify the material interface in the long time simulation [23,40]. Therefore, high-order and high-resolution schemes are required [53].

The high-order schemes, including the weighted essentially non-oscillatory (WENO) method [27,28,50], the discontinuous Galerkin (DG) method [52,8,18,24] and the spectral volume (SV) scheme [38], have been extended to solve compressible multi-component flows. Actually, these schemes can achieve arbitrary high order of accuracy in space. And considering the

\* Corresponding author.

E-mail addresses: [lishiyi14@tsinghua.org.cn](mailto:lishiyi14@tsinghua.org.cn) (S. Li), [dongmiluo@stu.xmu.edu.cn](mailto:dongmiluo@stu.xmu.edu.cn) (D. Luo), [jxqiu@xmu.edu.cn](mailto:jxqiu@xmu.edu.cn) (J. Qiu), [jiang@iapcm.ac.cn](mailto:jiang@iapcm.ac.cn) (S. Jiang), [chen\\_yibing@iapcm.ac.cn](mailto:chen_yibing@iapcm.ac.cn) (Y. Chen).

simplicity and easy implementation, they are often coupled with a multi-stage method for time evolution [18,38,12,55]. However, to achieve uniform arbitrary high order of accuracy in both space and time, it is recommended to use the one-stage methods such as the arbitrary derivative in space and time method (ADER) [65,15,16] and the high-order GKS (HGKS) [33,37,34].

ADER is a one-step and fully discrete Godunov approach. The predecessor of ADER is the generalized Riemann problem (GRP) solver, which solves the generalized Riemann problem with piecewise smooth initial data [3,30,6]. However, it's too sophisticated to design a higher than third-order GRP [30]. By introducing a linearization technique, ADER can achieve arbitrary high order of accuracy both in space and time in implement.

Instead of solving the traditional Riemann problem, the flux evaluation of HGKS initiates from the integral solution of the Bhatnagar-Gross-Krook (BGK) equation [68,69,54]. This mechanism renders HGKS as an accurate and robust solver for compressible flows [33,37,42,48,26]. Based on the Taylor expansion of the integral solution, the one-stage third-order and fourth-order HGKS methods have been developed in [33,41,37]. However, it will be very complex and time-consuming for a higher-order HGKS proposed by employing the higher-order Taylor expansion [34]. To overcome this difficulty, EHGKS is developed as an efficient and easy-implement one-stage gas-kinetic method to solve the Euler equations [34]. It can achieve arbitrary high order of accuracy in both space and time [34,35].

The extensions of GKS to multi-component flows include [31,32,36,38,44,47,67]. Some of them introduce spurious oscillations in the vicinity of material interfaces [47]. This drawback was induced by the two factors: firstly, the GKS flux solver inherently induces the spurious velocity and pressure oscillations in the vicinity of the contact discontinuity [9,10]; secondly, it also produces spurious oscillations to solve any conservative version of the additional equation to identify different components [1,10]. The modified KFVS (MKFVS) and NOK give a remedy for the first difficulty [9,10]. Then, following the idea of Abgrall's quasi-conservative method, a series of oscillation-free GKS are proposed for multi-component flows [10,38,40,39,2]. However, the schemes MKFVS and NOK are the first-order flux solver only. To the authors' best knowledge, all these schemes use the multi-stage method in time [10,38,40,39], which will definitely encounter the accuracy barrier [65,15,16]. In this paper, by coupling with NOK, EHGKS is extended to solve multi-component flows, which can not only achieve arbitrary high order of accuracy in both space and time, but also be oscillation-free for multi-component stiffened gases.

In the DIM framework, high-order schemes can significantly reduce the over diffusion of a material interface. But it's impossible to obtain a sharp interface without introducing an interface-sharpening technique. The traditional approaches include the level-set methods [17,14,46], the front tracking methods [62] and the volume of fraction or volume of fluid (VOF) methods [58–60,29,66,49,51,4,25]. These methods are either non-conservative, or somewhat complex because they have to introduce complex front tracking [62]/geometrical reconstruction computations [4,5,7,58] or additional interface compression/anti-diffusion source terms [64,53]. The algebraic type VOF methods evidently simplify the computational complexity and have attracted more practical interest in the recent years [59,13,61,11,70,22]. One of the most popular algebraic type VOF methods is THINC (tangent hyperbola for interface capturing), based on the use of hyperbolic tangent functions to approximate solutions with jump [59]. The drawback of THINC lies in the reconstruction of the multi-dimensional interface function, which can not be computed analytically. In this paper, to reduce the computational complexity, we develop, in addition, a novel simple interface-sharpening technique, by combining the idea of SLIC (simple line interface construction) [45], the ancestral VOF method and the downwind scheme.

This paper is organized as follows. Firstly, both EHGKS and NOK are briefly reviewed in Section 2. In Section 3, the construction of the new scheme is presented. Numerical examples are presented in Section 4 to validate the accuracy and resolution of the new scheme. A conclusion is made in the last section.

## 2. Review

### 2.1. EHGKS

EHGKS provides an efficient high-order flux solver for the Euler equations [34]. The one-dimensional Euler equations can be written as

$$\frac{\partial \mathbf{W}}{\partial t} + \frac{\partial \mathbf{F}}{\partial x} = \mathbf{0}. \quad (1)$$

Here  $\mathbf{W} = (\rho, \rho U, \rho E)$  and  $\mathbf{F} = (\rho U, \rho U^2 + p, \rho EU + pU)$ .  $\rho$ ,  $U$ ,  $p$  are the density, velocity and pressure, respectively.  $\rho E$  is the total energy.  $\rho e$  is the internal energy and  $E = \frac{1}{2}U^2 + e$ . For an ideal gas,  $p = (\gamma - 1)\rho e$ .  $\gamma$  is the specific heat ratio.

Under the finite volume framework, assume the space domain is discretized into  $N$  cells. The cell over  $[x_{i-\frac{1}{2}}, x_{i+\frac{1}{2}}]$  is indexed as  $i$ . The cell size is  $\Delta x = x_{i+\frac{1}{2}} - x_{i-\frac{1}{2}}$ . The time domain is discretized into  $0, \Delta t^0, \dots, t^n, t^{n+1} = t^n + \Delta t^n, \dots$ . Here we take  $\Delta t^n$  by  $\Delta t$  for simplicity.  $t^n = 0$  is adopted without loss of generality. The cell average of the variable  $\mathbf{W}(x, t)$  over the  $i$ -th cell at time  $t^n$  is recorded as  $\bar{\mathbf{W}}_i^n$ . Under the one-step fully discrete method, the cell averages of the conservative variables are updated by

$$\overline{\mathbf{W}}_i^{n+1} = \overline{\mathbf{W}}_i^n - \frac{1}{\Delta x} \left( \int_0^{\Delta t} \mathbf{F}_{i+\frac{1}{2}}(t) dt - \int_0^{\Delta t} \mathbf{F}_{i-\frac{1}{2}}(t) dt \right). \tag{2}$$

GKS uses the integral solution of the BGK equation to evaluate  $\mathbf{F}_{i+\frac{1}{2}}(t)$  [69]. EHGKS provides a simplification and modification on the integral solution for an efficient flux evaluation with arbitrary high order of accuracy, which is [34]

$$\mathbf{F}_{i+\frac{1}{2}}(t) = \left(1 - e^{-\frac{\Delta t}{\tau}}\right) \mathbf{F}^e(t) + e^{-\frac{\Delta t}{\tau}} \mathbf{F}^k(t). \tag{3}$$

$\mathbf{F}^e(t)$  is the term to guarantee EHGKS with arbitrary  $(r + 1)$ -th order of accuracy in smooth regions, which contains the leading term and high-order terms [34]:

$$\mathbf{F}^e(t) = \mathbb{F}^e + \sum_{l=1}^r \frac{t^l}{l!} \frac{\partial^l \mathbb{F}^e}{\partial t^l}, \tag{4}$$

where  $\mathbb{F}^e = (\rho U, \rho U^2 + p, \rho EU + pU)^e$ . The variables in  $\mathbb{F}^e$  are determined by  $\mathbb{W}^e = (\rho, \rho U, \rho E)^e$ , where  $\mathbb{W}^e = \mathbb{W}^{e+} + \mathbb{W}^{e-}$  and [69,34]

$$\begin{aligned} \mathbb{W}^{e\pm} &= \langle u^0 \rangle^\pm \begin{pmatrix} \rho \\ 0 \\ \rho e \end{pmatrix}_{i+\frac{1}{2}^\pm} + \langle u^1 \rangle^\pm \begin{pmatrix} 0 \\ \rho \\ \frac{1}{2} \rho U \end{pmatrix}_{i+\frac{1}{2}^\pm}, \\ \langle u^0 \rangle^\pm &= \frac{1}{2} \operatorname{erfc} \left( \pm \sqrt{\lambda_{i+\frac{1}{2}^\pm}} U_{i+\frac{1}{2}^\pm} \right), \\ \langle u^1 \rangle^\pm &= U_{i+\frac{1}{2}^\pm} \langle u^0 \rangle^\pm \mp \frac{1}{2} \frac{e^{-\lambda_{i+\frac{1}{2}^\pm} U_{i+\frac{1}{2}^\pm}^2}}{\sqrt{\pi \lambda_{i+\frac{1}{2}^\pm}}}. \end{aligned} \tag{5}$$

Here  $\lambda = \frac{\rho}{2p}$ .  $\mathbf{W}_{i+\frac{1}{2}^\pm} = (\rho, \rho U, \rho E)_{i+\frac{1}{2}^\pm}$  are the point-wise values after the reconstruction over the  $i$ -th and  $(i + 1)$ -th cell. See Appendix A for more details on the reconstruction. To obtain the temporal derivatives in Eq. (4), the state-of-art Lax-Wendroff procedure [21,63] is introduced in EHGKS. It is implemented based on the primary variables for simplicity [34].  $\mathbf{F}^k(t)$  in Eq. (3) is the low-order KFVS flux solver [34]. The first-order KFVS solver is [69,9]

$$\mathbf{F}^k(t) = \mathbb{F}^k, \tag{6}$$

where  $\mathbb{F}^k = \mathbb{F}^{k+} + \mathbb{F}^{k-}$  and

$$\mathbb{F}^{k\pm} = \langle u^1 \rangle^\pm \begin{pmatrix} \rho \\ \rho U \\ \rho E + \frac{1}{2} p \end{pmatrix}_{i+\frac{1}{2}^\pm} + \langle u^0 \rangle^\pm \begin{pmatrix} 0 \\ p \\ \frac{1}{2} p U \end{pmatrix}_{i+\frac{1}{2}^\pm}. \tag{7}$$

The weight between  $\mathbf{F}^e(t)$  and  $\mathbf{F}^k(t)$  is related to  $\tau$  [69]:

$$\tau = C_1 \Delta t + C_2 \left| \frac{p_{i+\frac{1}{2}^+} - p_{i+\frac{1}{2}^-}}{p_{i+\frac{1}{2}^+} + p_{i+\frac{1}{2}^-}} \right| \Delta t, \tag{8}$$

where  $C_1$  and  $C_2$  are two constant parameters;  $C_1 \ll 1$  and  $C_2 \sim O(1)$  [34,26]. In a smooth region where  $\tau \ll \Delta t$ ,  $\mathbf{F}_{i+\frac{1}{2}}(t) \approx \mathbf{F}^e(t)$  to obtain high accuracy. Near the discontinuities,  $\mathbf{F}_{i+\frac{1}{2}}(t)$  approaches to  $\mathbf{F}^k(t)$  for the robustness.

### 2.2. The 4-equations model and NOK

The 4-equations model is based on the extended Euler equations, such as with the equation of a mass fraction ( $Y$ ) [1,10,38]:

$$\frac{\partial Y}{\partial t} + \frac{\partial UY}{\partial x} = Y \frac{\partial U}{\partial x}. \tag{9}$$

The scheme for the equation of  $Y$  can be written by [1,10]

$$\begin{aligned} \bar{Y}_i^{n+1} = & \bar{Y}_i^n - \frac{1}{\Delta x} \left( \int_0^{\Delta t} F_{Y_{i+\frac{1}{2}}} (t) dt - \int_0^{\Delta t} F_{Y_{i-\frac{1}{2}}} (t) dt \right) \\ & + \bar{Y}_i^n \frac{1}{\Delta x} \left( \int_0^{\Delta t} U_{Y_{i+\frac{1}{2}}} (t) dt - \int_0^{\Delta t} U_{Y_{i-\frac{1}{2}}} (t) dt \right), \end{aligned} \tag{10}$$

where  $F_Y = UY$  and  $U_Y = U$ . The flux and source evaluations are [10,38]

$$\begin{aligned} F_{Y_{i+\frac{1}{2}}} (t) &= \left( 1 - e^{-\frac{\Delta t}{\tau}} \right) F_Y^e(t) + e^{-\frac{\Delta t}{\tau}} F_Y^k(t), \\ U_{Y_{i+\frac{1}{2}}} (t) &= \left( 1 - e^{-\frac{\Delta t}{\tau}} \right) U_Y^e(t) + e^{-\frac{\Delta t}{\tau}} U_Y^k(t). \end{aligned} \tag{11}$$

To avoid the velocity and pressure oscillations in the vicinity of the contact discontinuity, NOK provides a modification on the original first-order GKS by [9,10,40,38]

$$\begin{aligned} \mathbf{F}^e(t) &= \mathbb{F}^{e,\text{NOK}}, \\ \mathbf{F}^k(t) &= \mathbb{F}^{k,\text{NOK}}, \end{aligned} \tag{12}$$

where  $\mathbb{F}^{e,\text{NOK}} = (\rho U, \rho U^2 + p, \rho EU + pU)^{e,\text{NOK}}$ . The variables in  $\mathbb{F}^{e,\text{NOK}}$  are determined by  $\mathbb{Q}^{e,\text{NOK}} = (\rho, U, p)^{e,\text{NOK}}$ , where  $\mathbb{Q}^{e,\text{NOK}} = \mathbb{Q}^{e+,\text{NOK}} + \mathbb{Q}^{e-,\text{NOK}}$  and [10]

$$\mathbb{Q}^{e\pm,\text{NOK}} = \langle u^0 \rangle^{\pm,\text{NOK}} \begin{pmatrix} \rho \\ 0 \\ p \end{pmatrix}_{i+\frac{1}{2}^\pm} + \langle u^1 \rangle^{\pm,\text{NOK}} \begin{pmatrix} 0 \\ 1 \\ 0 \end{pmatrix}_{i+\frac{1}{2}^\pm}, \tag{13}$$

where  $\langle u^0 \rangle^{\pm,\text{NOK}}$  and  $\langle u^1 \rangle^{\pm,\text{NOK}}$  have the same expressions as Eq. (5) with  $\lambda_{i+\frac{1}{2}^\pm}$  replaced by [10]

$$\lambda_{i+\frac{1}{2}}^{\text{NOK}} = \min \left\{ \frac{1}{c_{i+\frac{1}{2}}^{2+}}, \frac{1}{c_{i+\frac{1}{2}}^{2-}} \right\},$$

with  $c$  being the speed of sound. For a stiffened gas,  $p = (\gamma - 1) \rho e - \gamma p_\infty$  and  $c = \sqrt{\frac{\gamma(p+p_\infty)}{\rho}}$  [56].  $\mathbb{F}^{k,\text{NOK}}$  has the same expression as Eq. (6) with  $\langle u^0 \rangle^\pm$  and  $\langle u^1 \rangle^\pm$  replaced by  $\langle u^0 \rangle^{\pm,\text{NOK}}$  and  $\langle u^1 \rangle^{\pm,\text{NOK}}$  respectively [10]. To solve the equation of the mass fraction, NOK follows the idea of Abgrall's 4-equations model [1] to guarantee oscillation-free across the material interface, which is [10]

$$\begin{aligned} F_Y^e(t) &= \mathbb{F}_Y^{e,\text{NOK}} = U^{e,\text{NOK}} Y^{e,\text{NOK}}, \\ F_Y^k(t) &= \mathbb{F}_Y^{k,\text{NOK}} = \langle u^1 \rangle^{+,\text{NOK}} Y_{i+\frac{1}{2}}^{+,\text{NOK}} + \langle u^1 \rangle^{-,\text{NOK}} Y_{i+\frac{1}{2}}^{-,\text{NOK}}, \\ U_Y^e(t) &= \mathbb{U}_Y^{e,\text{NOK}} = U^{e,\text{NOK}}, \\ U_Y^k(t) &= \mathbb{U}_Y^{k,\text{NOK}} = \langle u^1 \rangle^{+,\text{NOK}} + \langle u^1 \rangle^{-,\text{NOK}}, \end{aligned} \tag{14}$$

where  $Y^{e,\text{NOK}} = \langle u^0 \rangle^{+,\text{NOK}} Y_{i+\frac{1}{2}}^{+,\text{NOK}} + \langle u^0 \rangle^{-,\text{NOK}} Y_{i+\frac{1}{2}}^{-,\text{NOK}}$ . In multi-component flows,  $\gamma$  and  $p_\infty$  of the mixture are given by [1,56]

$$\begin{aligned} \frac{1}{\gamma - 1} &= \frac{1}{\gamma^{(1)} - 1} Y + \frac{1}{\gamma^{(2)} - 1} (1 - Y), \\ \frac{\gamma p_\infty}{\gamma - 1} &= \frac{\gamma^{(1)} p_\infty^{(1)}}{\gamma^{(1)} - 1} Y + \frac{\gamma^{(2)} p_\infty^{(2)}}{\gamma^{(2)} - 1} (1 - Y), \end{aligned} \tag{15}$$

where  $Y = 1$  denotes the first component, which is notated as (1);  $Y = 0$  denotes the second component, which is notated as (2).

**Remark 1.** EHGKS can achieve arbitrary high order of accuracy in both space and time, but is applicable only for a single ideal gas [34]. NOK is a modification of GKS to avoid the velocity and pressure oscillations in the vicinity of the contact discontinuity [9,10]. Based on Abgrall's 4-equations model, it's straight-forward to extend NOK for multi-component flows with no spurious pressure oscillations across the material interface [10,38,40]. However, NOK provides only a first-order flux solver. The existing schemes using the NOK flux solver are built under the multi-stage framework to obtain high order of temporal accuracy [38,40,39].

### 3. MEHGKS: EHGKS for multi-component stiffened gases

In this section, EHGKS is extended for the 4-equations model of compressible multi-component stiffened gases. A straight-forward way to preserve high order of accuracy in smooth regions and without spurious velocity and pressure oscillations across a material interface is to replace  $\mathbb{F}^e$  by  $\mathbb{F}^{e,\text{NOK}}$  and  $\mathbb{F}^k$  by  $\mathbb{F}^{k,\text{NOK}}$ . To further reduce the over diffusion near the material interface, a simple interface-sharpening technique is also proposed, which combines the idea of VOF-SLIC [45] and a downwind scheme. These two methods are illustrated in the following respectively.

#### 3.1. MEHGKS for multi-component flows with uniform high order of accuracy in both space and time

This part introduces a combination of EHGKS and NOK with careful treatment, firstly to avoid the spurious velocity and pressure oscillations across a material interface, and secondly to achieve high order of accuracy in both space and time in smooth regions.

The flux and source evaluations are based on Eqs. (3) and (11). To avoid the spurious velocity and pressure oscillations across the contact discontinuity, it's possible to give

$$\begin{aligned} \mathbf{F}^e(t) &= \mathbb{F}^{k,\text{NOK}} + \sum_{l=1}^r \frac{t^l}{l!} \frac{\partial^l \mathbb{F}^{e,\text{NOK}}}{\partial t^l}, \\ \mathbf{F}^k(t) &= \mathbb{F}^{k,\text{NOK}}. \end{aligned} \tag{16}$$

The high-order terms are included in  $\mathbf{F}^e(t)$  to achieve high accuracy in the smooth regions of a pure material. The leading term  $\mathbb{F}^{k,\text{NOK}}$  works near the discontinuity to provide the robustness. According to the idea in [1], to avoid the spurious velocity and pressure oscillations across a material interface, the following condition should be satisfied: assuming that the velocity and pressure are constant at the  $n$ -th time step, i.e.,

$$\begin{aligned} \bar{U}_i^n &= U_0, \\ \bar{p}_i^n &= p_0, \end{aligned} \tag{17}$$

for  $i = 1, 2, \dots, N$ , then they should keep constant at the next time step:

$$\begin{aligned} \bar{U}_i^{n+1} &= U_0, \\ \bar{p}_i^{n+1} &= p_0. \end{aligned} \tag{18}$$

To simplify the notations, we introduce  $\nabla Q = Q_{i+\frac{1}{2}} - Q_{i-\frac{1}{2}}$ .  $Q$  can be any quantity. The traditional WENO method is implemented based on the primary variables for reconstruction, which can be referred in Appendix A. The reconstruction then gives  $U_{i+\frac{1}{2}}^\pm = U_0$  and  $p_{i+\frac{1}{2}}^\pm = p_0$ .  $\langle u^0 \rangle^{\pm,\text{NOK}}$  and  $\langle u^1 \rangle^{\pm,\text{NOK}}$  thus have the following properties [38]:

$$\begin{aligned} \langle u^0 \rangle^{+,\text{NOK}} + \langle u^0 \rangle^{-,\text{NOK}} &= 1, \\ \langle u^1 \rangle^{+,\text{NOK}} + \langle u^1 \rangle^{-,\text{NOK}} &= U_0. \end{aligned} \tag{19}$$

$\tau$  is then  $\tau = C_1 \Delta t$ . After some algebraic simplifications on Eqs. (2) and (10),  $\bar{\rho}_i^{n+1}$  is updated by

$$\bar{\rho}_i^{n+1} = \bar{\rho}_i^n - \frac{\Delta t}{\Delta x} \left( \nabla \mathbb{F}(1)^{k,\text{NOK}} + U_0 \left( 1 - e^{-\frac{1}{c_1}} \right) \sum_{l=1}^r \frac{\Delta t^l}{(l+1)!} \frac{\partial^l \nabla \rho^{e,\text{NOK}}}{\partial t^l} \right), \tag{20}$$

$\bar{\rho} U_i^{n+1}$  is updated by

$$\bar{\rho} U_i^{n+1} = \bar{\rho}_i^n U_0 - \frac{U_0 \Delta t}{\Delta x} \left( \nabla \mathbb{F}(1)^{k,\text{NOK}} + U_0 \left( 1 - e^{-\frac{1}{c_1}} \right) \sum_{l=1}^r \frac{\Delta t^l}{(l+1)!} \frac{\partial^l \nabla \rho^{e,\text{NOK}}}{\partial t^l} \right), \tag{21}$$

and  $\bar{\rho} E_i^{n+1}$  is updated by

$$\bar{\rho} E_i^{n+1} = \bar{\rho} E_i^n - \frac{\Delta t}{\Delta x} \left( \nabla \mathbb{F}(3)^{k,\text{NOK}} + U_0 \left( 1 - e^{-\frac{1}{c_1}} \right) \sum_{l=1}^r \frac{\Delta t^l}{(l+1)!} \frac{\partial^l \nabla (\rho^{e,\text{NOK}} E^{e,\text{NOK}})}{\partial t^l} \right). \tag{22}$$

After substituting Eq. (20) to Eq. (21), we can get obviously

$$\bar{U}_i^{n+1} = \frac{\bar{\rho}U_i^{n+1}}{\bar{\rho}_i^{n+1}} = U_0.$$

After substituting Eq. (20) and Eq. (15) into Eq. (22), the condition  $\bar{p}_i^{n+1} = p_0$  is preserved by

$$\bar{Y}_i^{n+1} = \bar{Y}_i^n - \frac{\Delta t}{\Delta x} \left( \nabla \mathbb{F}_Y^{k,\text{NOK}} + U_0 \left( 1 - e^{-\frac{1}{c_1}} \right) \sum_{l=1}^r \frac{\Delta t^l}{(l+1)!} \frac{\partial^l \nabla Y^{e,\text{NOK}}}{\partial t^l} \right). \tag{23}$$

The details of the derivation can be referred in Appendix B. If we take the same expressions as Eq. (11), this condition is also satisfied by the following flux and source evaluations:

$$\begin{aligned} F_Y^e(t) &= \mathbb{F}_Y^{k,\text{NOK}} + \sum_{l=1}^r \frac{t^l}{l!} \frac{\partial^l \mathbb{F}_Y^{e,\text{NOK}}}{\partial t^l}, \\ F_Y^k(t) &= \mathbb{F}_Y^{k,\text{NOK}}, \\ U_Y^e(t) &= \mathbb{U}_Y^{k,\text{NOK}} + \sum_{l=1}^r \frac{t^l}{l!} \frac{\partial^l \mathbb{U}_Y^{e,\text{NOK}}}{\partial t^l}, \\ U_Y^k(t) &= \mathbb{U}_Y^{k,\text{NOK}}. \end{aligned} \tag{24}$$

The Lax-Wendroff procedure to obtain the temporal derivatives is replaced by:

$$\begin{aligned} \frac{\partial^{m+l}}{\partial x^m \partial t^l} \left( \frac{\partial}{\partial t} \left( \frac{Q}{Y} \right)^{e,\text{NOK}} + \mathbb{A}^{e,\text{NOK}} \cdot \frac{\partial}{\partial x} \left( \frac{Q}{Y} \right)^{e,\text{NOK}} \right) &= \mathbf{0}, \\ \mathbb{A} &= \begin{bmatrix} U & \rho & 0 & 0 \\ 0 & U & 1/\rho & 0 \\ 0 & \gamma(p + p_\infty) & U & 0 \\ 0 & 0 & 0 & U \end{bmatrix}. \end{aligned} \tag{25}$$

Here  $m + l = 0, 1, \dots, r - 1$ .

As a summary, Eqs. (16) and (24) provide the flux and source evaluations of the currently constructed scheme, which is called MEHGKS in this work.

**Remark 2.** MEHGKS is applicable for stiffened gases, with uniform high order of accuracy in both space and time in smooth regions of a pure material. To simulate multi-component flows, MEHGKS can avoid the spurious velocity and pressure oscillations across material interfaces. However, MEHGKS, as a DIM, presents over diffusion of material interfaces. An interface-sharpening technique is developed in the following to preserve MEHGKS with high resolution on material interfaces.

### 3.2. MEHGKS for multi-component flows with high resolution on material interfaces

In this part, a simple and effective interface-sharpening technique is developed under the framework of MEHGKS. The new technique takes the advantages of both the traditional VOF method, which possesses high resolution but introduces complex geometric intersection operations [45,58], and the downwind method, which is simple but unstable if without restrictions. In the new method, SLIC [45] is firstly used to track the movement of a material interface. Tracking the movement takes only simple geometric calculations, without the complex intersection operations in the complete VOF method [45,58]. Based on the movement of the material interface, a novel restriction is then given on the downwind scheme to preserve the robustness. The details are given in the following.

#### (1). Track the movement of a material interface.

We use the condition  $(\bar{Y}_i^n - \bar{Y}_{i+1}^n)(\bar{Y}_{i-1}^n - \bar{Y}_i^n) > 0$  to indicate the existence of a material interface within the  $i$ -th cell. According to the idea of SLIC [45], a jump in mass fraction is assumed in this cell to divide the two components, which locates at

$$x_{i,Y}^n = x_{i-\frac{1}{2}} + \frac{\bar{Y}_i^n - \bar{Y}_{i+1}^n}{\bar{Y}_{i-1}^n - \bar{Y}_{i+1}^n} \Delta x.$$

By evaluating with first-order of accuracy, the material interface moves at a speed of  $\bar{U}_i^n$  from  $t^n$  to  $t^{n+1}$ . The location of the jump at  $t^{n+1}$  is then

$$x_{i,Y}^{n+1} = x_{i-\frac{1}{2}} + \frac{\bar{Y}_i^n - \bar{Y}_{i+1}^n}{\bar{Y}_{i-1}^n - \bar{Y}_{i+1}^n} \Delta x + \bar{U}_i^n \Delta t.$$

Similarly, if the jump is evaluated by density, the location of the jump at  $t^{n+1}$  will be

$$x_{i,\rho}^{n+1} = x_{i-\frac{1}{2}} + \frac{\bar{\rho}_i^n - \bar{\rho}_{i+1}^n}{\bar{\rho}_{i-1}^n - \bar{\rho}_{i+1}^n} \Delta x + \bar{U}_i^n \Delta t.$$

(2). Reconstruct the point-wise density and mass fraction.

After the WENO reconstruction in MEHGKS, the point-wise density and mass fraction are modified if the updated jump remains in the  $i$ -th cell. That is, if  $x_{i,\rho}^{n+1}$  and  $x_{i,Y}^{n+1}$  are below  $x_{i+\frac{1}{2}}$ , the point-wise density and mass fraction are modified by the cell averages in the  $(i + 1)$ -th cell, i.e.,

$$\begin{pmatrix} \rho \\ Y \end{pmatrix}_{i+\frac{1}{2}^-} = \begin{pmatrix} \bar{\rho}_{i+1}^n \\ \bar{Y}_{i+1}^n \end{pmatrix}, \quad \text{if } x_{i,\rho}^{n+1} < x_{i+\frac{1}{2}} \text{ and } x_{i,Y}^{n+1} < x_{i+\frac{1}{2}}; \tag{26}$$

if  $x_{i,\rho}^{n+1}$  and  $x_{i,Y}^{n+1}$  are above  $x_{i-\frac{1}{2}}$ , the point-wise density and mass fraction are modified by the  $(i - 1)$ -th cell averages, i.e.,

$$\begin{pmatrix} \rho \\ Y \end{pmatrix}_{i-\frac{1}{2}^+} = \begin{pmatrix} \bar{\rho}_{i-1}^n \\ \bar{Y}_{i-1}^n \end{pmatrix}, \quad \text{if } x_{i,\rho}^{n+1} > x_{i-\frac{1}{2}} \text{ and } x_{i,Y}^{n+1} > x_{i-\frac{1}{2}}. \tag{27}$$

The above reconstruction acts only near material interfaces where  $|\bar{Y}_{i+1}^n - \bar{Y}_i^n| > \epsilon$  or  $|\bar{Y}_{i-1}^n - \bar{Y}_i^n| > \epsilon$ . If else, it remains to the former MEHGKS. Following the idea in [22], only the density and mass fraction, which vary across a material interface, are modified. It should be mentioned that the present method results in an unstable downwind scheme if without the restrictions in Eqs. (26)-(27). The novel restriction is given based on the movement of an evaluated material interface in order to preserve the robustness. The new method thus possesses: (1) stability under the restrictions; (2) high resolution near material interfaces which is initiated from both VOF and the downwind scheme; (3) simplicity compared to the traditional VOF method.

To enhance the robustness of the method with the new interface-sharpening technique, the leading terms in the original flux and source evaluations of MEHGKS are replaced by

$$\begin{aligned} \mathbf{F}^k(t) &= \left(1 - e^{-\frac{\Delta t}{\tau^*}}\right) \mathbb{F}^{k,\text{NOK}} + e^{-\frac{\Delta t}{\tau^*}} \mathcal{F}, \\ F_Y^k(t) &= \left(1 - e^{-\frac{\Delta t}{\tau^*}}\right) \mathbb{F}_Y^{k,\text{NOK}} + e^{-\frac{\Delta t}{\tau^*}} \mathcal{F}_Y, \\ U_Y^k(t) &= \left(1 - e^{-\frac{\Delta t}{\tau^*}}\right) \mathbb{U}_Y^{k,\text{NOK}} + e^{-\frac{\Delta t}{\tau^*}} \mathcal{U}_Y, \end{aligned} \tag{28}$$

where

$$\begin{aligned} \mathcal{F} &= \frac{1 + \text{sign}(\tilde{U})}{2} \mathcal{F}^- + \frac{1 - \text{sign}(\tilde{U})}{2} \mathcal{F}^+, \\ \mathcal{F}_Y &= \frac{1 + \text{sign}(\tilde{U})}{2} \mathcal{F}_Y^- + \frac{1 - \text{sign}(\tilde{U})}{2} \mathcal{F}_Y^+, \\ \mathcal{U}_Y &= \frac{1 + \text{sign}(\tilde{U})}{2} \mathcal{U}_Y^- + \frac{1 - \text{sign}(\tilde{U})}{2} \mathcal{U}_Y^+, \end{aligned} \tag{29}$$

and

$$\begin{aligned} \mathcal{F}^\pm &= \tilde{U} \begin{pmatrix} \rho \\ \rho U \\ \rho E \end{pmatrix}_{i+\frac{1}{2}^\pm} + \begin{pmatrix} 0 \\ \tilde{p} \\ \tilde{p} \tilde{U} \end{pmatrix}, \\ \mathcal{F}_Y^\pm &= \tilde{U} Y_{i+\frac{1}{2}^\pm}, \\ \mathcal{U}_Y^\pm &= \tilde{U}. \end{aligned} \tag{30}$$

$\mathcal{F}$ ,  $\mathcal{F}_Y$  and  $\mathcal{U}_Y$  are given by a simple splitting technique. The velocity  $\tilde{U}$  and pressure  $\tilde{p}$  are evaluated by the acoustic impedance and inverse interpolation respectively with artificial viscosity [43]:

$$\begin{aligned} \tilde{U} &= \frac{(\rho c U)_{i+\frac{1}{2}}^-}{(\rho c)_{i+\frac{1}{2}}^- + (\rho c)_{i+\frac{1}{2}}^+} + \frac{(\rho c U)_{i+\frac{1}{2}}^+}{(\rho c)_{i+\frac{1}{2}}^- + (\rho c)_{i+\frac{1}{2}}^+} - \Delta t \frac{p_{i+\frac{1}{2}}^+ - p_{i+\frac{1}{2}}^-}{\rho_{i+\frac{1}{2}}^- + \rho_{i+\frac{1}{2}}^+}, \\ \tilde{p} &= \frac{(\rho c)_{i+\frac{1}{2}}^- p_{i+\frac{1}{2}}^+}{(\rho c)_{i+\frac{1}{2}}^- + (\rho c)_{i+\frac{1}{2}}^+} + \frac{(\rho c)_{i+\frac{1}{2}}^+ p_{i+\frac{1}{2}}^-}{(\rho c)_{i+\frac{1}{2}}^- + (\rho c)_{i+\frac{1}{2}}^+} \\ &+ \begin{cases} 0, U_{i+\frac{1}{2}}^+ - U_{i+\frac{1}{2}}^- \geq 0 \\ 0.3 \times (\rho_{i+\frac{1}{2}}^+ + \rho_{i+\frac{1}{2}}^-) (U_{i+\frac{1}{2}}^+ - U_{i+\frac{1}{2}}^-)^2, U_{i+\frac{1}{2}}^+ - U_{i+\frac{1}{2}}^- < 0 \end{cases}. \end{aligned}$$

The resultant scheme, called MEHGKS-IS, utilizes the new reconstruction, flux and source solvers which act only near a material interface. It remains to the original MEHGKS elsewhere. The weight in the new solver is related to  $\tau^*$ :

$$\tau^* = C_3 \left| \bar{Y}_i^n - \bar{Y}_{i+1}^n \right| \Delta t. \tag{31}$$

$C_3$  is a constant.

**Remark 3.** To simulate immiscible multi-component flows, MEHGKS-IS is developed to preserve not only high order of accuracy in both space and time in smooth regions of a pure material, but also high resolution near material interfaces.

### 3.3. The two-dimensional case

In this section, MEHGKS and MEHGKS-IS are extended to the two-dimensional case. In the two-dimensional case, the 4-equations model is updated by

$$\begin{aligned} \begin{pmatrix} \bar{\mathbf{W}}_{i,j}^{n+1} \\ \bar{Y}_{i,j}^{n+1} \end{pmatrix} &= \begin{pmatrix} \bar{\mathbf{W}}_{i,j}^n \\ \bar{Y}_{i,j}^n \end{pmatrix} - \frac{1}{\Delta x} \int_0^{\Delta t} \left( \begin{pmatrix} \mathbf{F}_{i+\frac{1}{2},j}(t) \\ F_{Y_{i+\frac{1}{2},j}}(t) \end{pmatrix} - \begin{pmatrix} \mathbf{F}_{i-\frac{1}{2},j}(t) \\ F_{Y_{i-\frac{1}{2},j}}(t) \end{pmatrix} \right) dt \\ &\quad - \frac{1}{\Delta y} \int_0^{\Delta t} \left( \begin{pmatrix} \mathbf{G}_{i,j+\frac{1}{2}}(t) \\ G_{Y_{i,j+\frac{1}{2}}}(t) \end{pmatrix} - \begin{pmatrix} \mathbf{G}_{i,j-\frac{1}{2}}(t) \\ G_{Y_{i,j-\frac{1}{2}}}(t) \end{pmatrix} \right) dt \\ &\quad + \bar{Y}_{i,j}^n \frac{1}{\Delta x} \int_0^{\Delta t} \left( \begin{pmatrix} \mathbf{0} \\ U_{Y_{i+\frac{1}{2},j}}(t) \end{pmatrix} - \begin{pmatrix} \mathbf{0} \\ U_{Y_{i-\frac{1}{2},j}}(t) \end{pmatrix} \right) dt \\ &\quad + \bar{Y}_{i,j}^n \frac{1}{\Delta y} \int_0^{\Delta t} \left( \begin{pmatrix} \mathbf{0} \\ V_{Y_{i,j+\frac{1}{2}}}(t) \end{pmatrix} - \begin{pmatrix} \mathbf{0} \\ V_{Y_{i,j-\frac{1}{2}}}(t) \end{pmatrix} \right) dt. \end{aligned} \tag{32}$$

Here  $\mathbf{W} = (\rho, \rho U, \rho V, \rho E)$  and  $\mathbf{F} = (\rho U, \rho U^2 + p, \rho UV, \rho EU + pU)$ .  $\mathbf{F}_{i+\frac{1}{2},j}(t)$ ,  $F_{Y_{i+\frac{1}{2},j}}(t)$  and  $U_{Y_{i+\frac{1}{2},j}}(t)$  have the similar form to Eqs. (3) and (11). The high-order terms in the flux and source evaluations are

$$\begin{aligned} \mathbf{F}^e(t) &= \mathbb{F}^{k,\text{NOK}} + \sum_{l=1}^r \frac{1}{l!} \left( t \frac{\partial}{\partial t} + y \frac{\partial}{\partial y} \right)^l \mathbb{F}^{e,\text{NOK}}, \\ F_Y^e(t) &= \mathbb{F}_Y^{k,\text{NOK}} + \sum_{l=1}^r \frac{1}{l!} \left( t \frac{\partial}{\partial t} + y \frac{\partial}{\partial y} \right)^l \mathbb{F}_Y^{e,\text{NOK}}, \\ U_Y^e(t) &= \mathbb{U}_Y^{k,\text{NOK}} + \sum_{l=1}^r \frac{1}{l!} \left( t \frac{\partial}{\partial t} + y \frac{\partial}{\partial y} \right)^l \mathbb{U}_Y^{e,\text{NOK}}. \end{aligned} \tag{33}$$

The Lax-Wendroff procedure to obtain the temporal derivatives reads as

$$\frac{\partial^{m+l+q}}{\partial x^m \partial y^l \partial t^q} \left( \frac{\partial}{\partial t} \begin{pmatrix} \mathbf{Q} \\ \mathbf{Y} \end{pmatrix}^{e,\text{NOK}} + \mathbb{A}^{e,\text{NOK}} \cdot \frac{\partial}{\partial x} \begin{pmatrix} \mathbf{Q} \\ \mathbf{Y} \end{pmatrix}^{e,\text{NOK}} + \mathbb{B}^{e,\text{NOK}} \cdot \frac{\partial}{\partial y} \begin{pmatrix} \mathbf{Q} \\ \mathbf{Y} \end{pmatrix}^{e,\text{NOK}} \right) = \mathbf{0},$$

$$\mathbb{A} = \begin{bmatrix} U & \rho & 0 & 0 & 0 \\ 0 & U & 0 & 1/\rho & 0 \\ 0 & 0 & U & 0 & 0 \\ 0 & \gamma(p + p_\infty) & 0 & U & 0 \\ 0 & 0 & 0 & 0 & U \end{bmatrix}, \mathbb{B} = \begin{bmatrix} V & 0 & \rho & 0 & 0 \\ 0 & V & 0 & 0 & 0 \\ 0 & 0 & V & 1/\rho & 0 \\ 0 & 0 & \gamma(p + p_\infty) & V & 0 \\ 0 & 0 & 0 & 0 & V \end{bmatrix}. \tag{34}$$

Here  $m + l + q = 0, 1, \dots, r - 1$ . The terms  $\mathbf{F}^k(t)$ ,  $F_Y^k(t)$  and  $U_Y^k(t)$  are given as follows.

(1). In MEHGKS, they are given by

$$\begin{aligned} \mathbf{F}^k(t) &= \mathbb{F}^{k,\text{NOK}}, \\ F_Y^k(t) &= \mathbb{F}_Y^{k,\text{NOK}}, \\ U_Y^k(t) &= \mathbb{U}_Y^{k,\text{NOK}}. \end{aligned} \tag{35}$$

(2). In MEHGKS-IS, they are given by

$$\begin{aligned} \mathbf{F}^k(t) &= \left(1 - e^{-\frac{\Delta t}{\tau^*}}\right) \mathbb{F}^{k,\text{NOK}} + e^{-\frac{\Delta t}{\tau^*}} \mathcal{F}, \\ F_Y^k(t) &= \left(1 - e^{-\frac{\Delta t}{\tau^*}}\right) \mathbb{F}_Y^{k,\text{NOK}} + e^{-\frac{\Delta t}{\tau^*}} \mathcal{F}_Y, \\ U_Y^k(t) &= \left(1 - e^{-\frac{\Delta t}{\tau^*}}\right) \mathbb{U}_Y^{k,\text{NOK}} + e^{-\frac{\Delta t}{\tau^*}} \mathcal{U}_Y, \end{aligned} \tag{36}$$

where  $\mathcal{F}$ ,  $\mathcal{F}_Y$  and  $\mathcal{U}_Y$  have the same expressions as Eq. (29) with  $\mathcal{F}^\pm$  replaced by

$$\mathcal{F}^\pm = \tilde{U} \begin{pmatrix} \rho \\ \rho U \\ \rho V \\ \rho E \end{pmatrix}_{i+\frac{1}{2}^\pm, j} + \begin{pmatrix} 0 \\ \tilde{p} \\ 0 \\ \tilde{p}\tilde{U} \end{pmatrix}.$$

Following the idea in [71], we take a simple and effective weight for  $\tau^*$ :

$$\tau^* = C_3 \frac{\Delta Y_x}{\Delta Y_x + \Delta Y_y} \Delta t, \tag{37}$$

where

$$\begin{aligned} \Delta Y_x &= \frac{1}{3} \sum_{k=-1}^1 \left| \bar{Y}_{i,j+k}^n - \bar{Y}_{i+1,j+k}^n \right|, \\ \Delta Y_y &= \sum_{l=0}^1 \sum_{k=-2}^1 \left| \bar{Y}_{i+l,j+k+1}^n - \bar{Y}_{i+l,j+k}^n \right|. \end{aligned}$$

$\mathbf{G}_{i,j+\frac{1}{2}}(t)$ ,  $G_{Y_{i,j+\frac{1}{2}}}(t)$  and  $V_{Y_{i,j+\frac{1}{2}}}(t)$  take the same form as  $\mathbf{F}_{i+\frac{1}{2},j}(t)$ ,  $F_{Y_{i+\frac{1}{2},j}}(t)$  and  $U_{Y_{i+\frac{1}{2},j}}(t)$  after transformation to the local normal direction.

#### 4. Numerical tests

The time step  $\Delta t$  is determined by the CFL condition [34,35]

$$\Delta t = CFL \times \min \left\{ \frac{\Delta x}{|\bar{U}| + \bar{c}}, \frac{\Delta y}{|\bar{V}| + \bar{c}} \right\}, \tag{38}$$

where we take  $CFL = 0.4$  if without specification.  $C_1 = 0.05$  (Eq. (8)),  $C_2 = 5$  (Eq. (8)) and  $C_3 = 50$  (Eq. (31), Eq. (37)) are adopted in this work [26].  $\epsilon = 10^{-3}$  is taken to identify a material interface. The results are not sensitive to  $\epsilon$ . The details are given in Appendix C. The numerical results of the  $r$ -th-order MEHGKS which is noted as MEHGKS- $r$ , and MEHGKS-IS which is noted as MEHGKS- $r$ -IS are performed. The reference solution is calculated under refined grids. The calculations are dimensionless. A number of one-dimensional and two-dimensional benchmark tests are carried out.

**Table 1**  
Accuracy test for MEHGKS in the one-dimensional advection of density perturbation.

MEHGKS-3						
$N$	$L_1$ error	Order	$L_2$ error	Order	$L_\infty$ error	Order
10	1.57E-02		1.72E-02		2.49E-02	
20	2.15E-03	2.87	2.39E-03	2.85	3.54E-03	2.81
40	2.73E-04	2.98	3.05E-04	2.97	4.61E-04	2.94
80	3.43E-05	2.99	3.83E-05	2.99	5.81E-05	2.99
MEHGKS-5						
$N$	$L_1$ error	Order	$L_2$ error	Order	$L_\infty$ error	Order
10	1.32E-03		1.44E-03		2.13E-03	
20	4.39E-05	4.91	4.88E-05	4.89	7.29E-05	4.87
40	1.39E-06	4.98	1.55E-06	4.97	2.35E-06	4.95
80	4.38E-08	4.99	4.88E-08	4.99	7.40E-08	4.99

4.1. The one-dimensional accuracy test

In this case, we assess the accuracy of MEHGKS in the smooth linear advection of density perturbation in a single stiffened gas [47]. The initial condition is given by

$$(\rho, U, p) = (1 + 0.2 \sin x, 1, 1).$$

$\gamma = 1.4$ .  $p_\infty = 1$ . Under the periodic boundary condition, the analytic solution is

$$(\rho, U, p) = (1 + 0.2 \sin(x - t), 1, 1).$$

The computational domain is  $[0, 2\pi]$  divided by  $N$  uniform cells. The output time is  $2\pi$ . To test the accuracy in both space and time, we take  $CFL = 0.9$  in this case.

The results of the errors and the accuracy order computed by MEHGKS-3 and MEHGKS-5 are shown in Table 1. All the MEHGKS-r schemes can achieve the designed order of accuracy in both space and time.

4.2. The interface only problem

This case contains an interface propagating at a constant speed to verify MEHGKS with no spurious velocity and pressure oscillations across a material interface. The initial condition is [56]

$$(\rho, U, p, \gamma, p_\infty) = \begin{cases} (1, 1, 1, 4, 1), & x < 0.2, \\ (0.125, 1, 1, 1.4, 0), & \text{else.} \end{cases}$$

The computational domain  $[0, 1]$ . The output time is 0.12. 100 uniform cells are used in this simulation [56].

Fig. 1 shows the results given by MEHGKS-3, MEHGKS-5 and MEHGKS-5-IS. The velocity and pressure are confirmed to be oscillation-free across the material interface. It also shows that MEHGKS-5 resolves the interface sharper than MEHGKS-3, illustrating the advantage of the higher accuracy. MEHGKS-5-IS gives the sharpest interface, and this demonstrates the high resolution of MEHGKS-5-IS.

4.3. The square wave propagation problem

This case contains a square wave propagating at a constant speed to assess the accuracy and resolution of the scheme [38,59]. The initial condition is given by

$$(\rho, U, p, \gamma, p_\infty) = \begin{cases} (1, 1, 1, 1.4, 0), & 0.3 \leq x \leq 0.7, \\ (5, 1, 1, 4, 1), & \text{else,} \end{cases}$$

with periodic boundary conditions on both sides of the computational domain  $[0, 1]$ . 20, 40 and 80 uniform cells are used. The output time of 100 periods is taken in this case for long time evolution.

Fig. 2 shows the results given by MEHGKS-3, MEHGKS-5 and MEHGKS-5-IS. They demonstrate the advantage of the high accuracy and high resolution of MEHGKS-5-IS in capturing a sharp interface. The velocity and pressure are also confirmed to be oscillation-free across a material interface.

4.4. The gas-helium shock tube problem

The initial conditions are given by [60]

$$(\rho, U, p, \gamma, p_\infty) = \begin{cases} (1, 0, 1, 1.4, 0), & x \leq 0.5, \\ (0.125, 0, 0.1, 1.667, 0), & \text{else.} \end{cases}$$

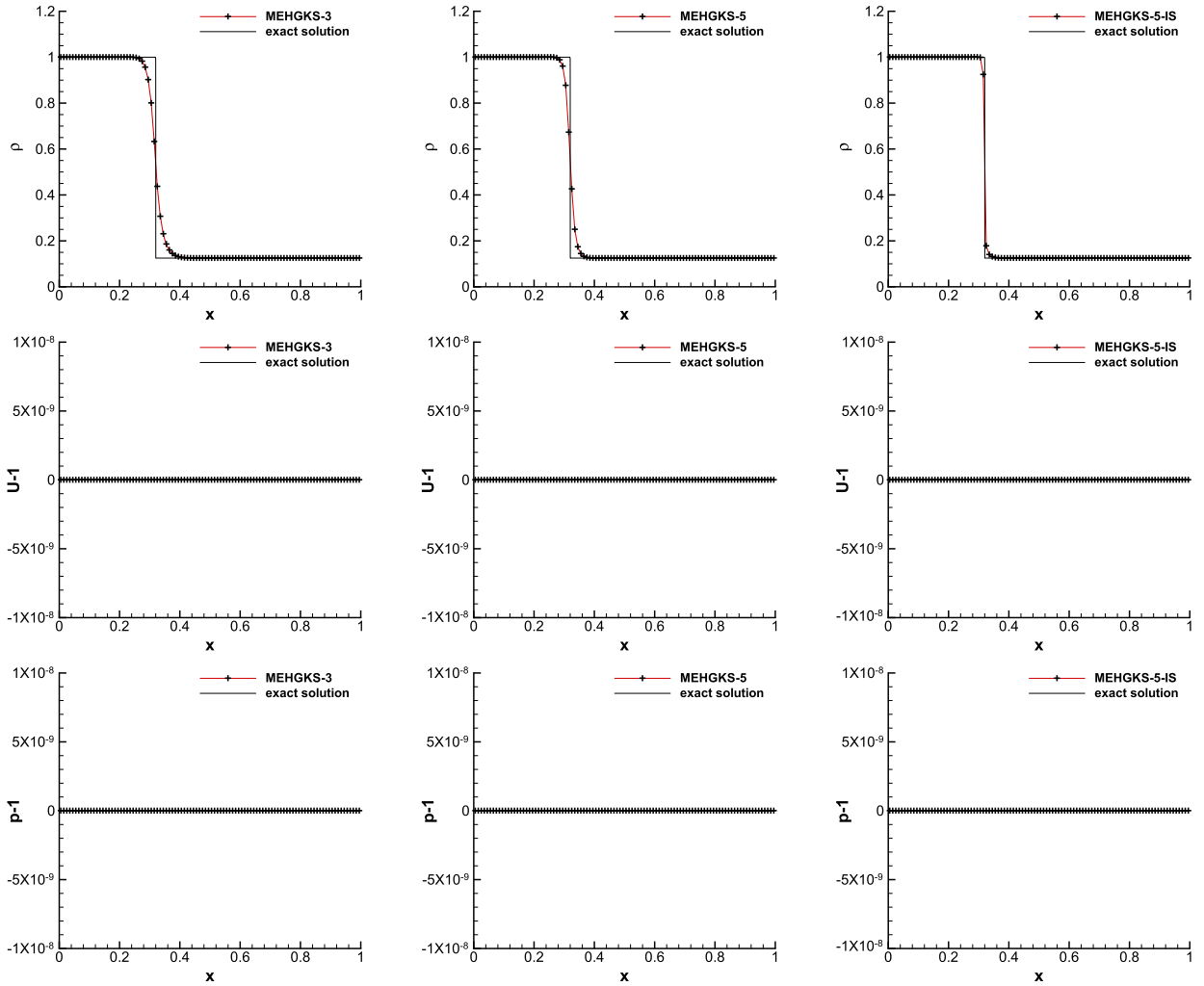


Fig. 1.  $\rho$ ,  $U$  and  $p$  of the interface only problem with 100 uniform cells at  $t = 0.12$ .

The computational domain is  $[0, 1]$ . The output time  $t = 0.15$ . 400 uniform cells are used [60].

Fig. 3 shows the result given by MEHGKS-3, MEHGKS-5 and MEHGKS-5-IS. It confirms the resolution of MEHGKS-5-IS better than MEHGKS-5, and MEHGKS-5 better than MEHGKS-3.

#### 4.5. The gas-liquid shock tube problems

Three different initial conditions of the gas-liquid shock tube problem are tested. The computational domain is  $[0, 1]$ . In the first case, the initial conditions are given by [56]

$$(\rho, U, p, \gamma, p_\infty) = \begin{cases} (1.241, 0, 2.753, 1.4, 0), & x < 0.5, \\ (0.991, 0, 3.059 \times 10^{-4}, 5.5, 1.505), & \text{else.} \end{cases}$$

The output time  $t = 0.1$ . 1000 uniform cells are used. In the second case, the initial conditions are given by [56]

$$(\rho, U, p, \gamma, p_\infty) = \begin{cases} (1, 0, 1, 1.4, 0), & x < 0.5, \\ (5, 0, 1, 4, 1), & 0.5 \leq x < 0.6, \\ (7.093, -0.7288, 10, 4, 1), & \text{else.} \end{cases}$$

The output time  $t = 0.2$ . 1000 uniform cells are used. The third case is a gas-liquid shock tube problem with large pressure ratio [57,29,38]. It will be very challenging with a strong shock wave while the shock and the material interface are very close [38]. The initial conditions are given by

$$(\rho, U, p, \gamma, p_\infty) = \begin{cases} (10^3, 0, 10^9, 4.4, 6 \times 10^8), & x \leq 0.6, \\ (50, 0, 10^5, 1.4, 0), & \text{else.} \end{cases}$$

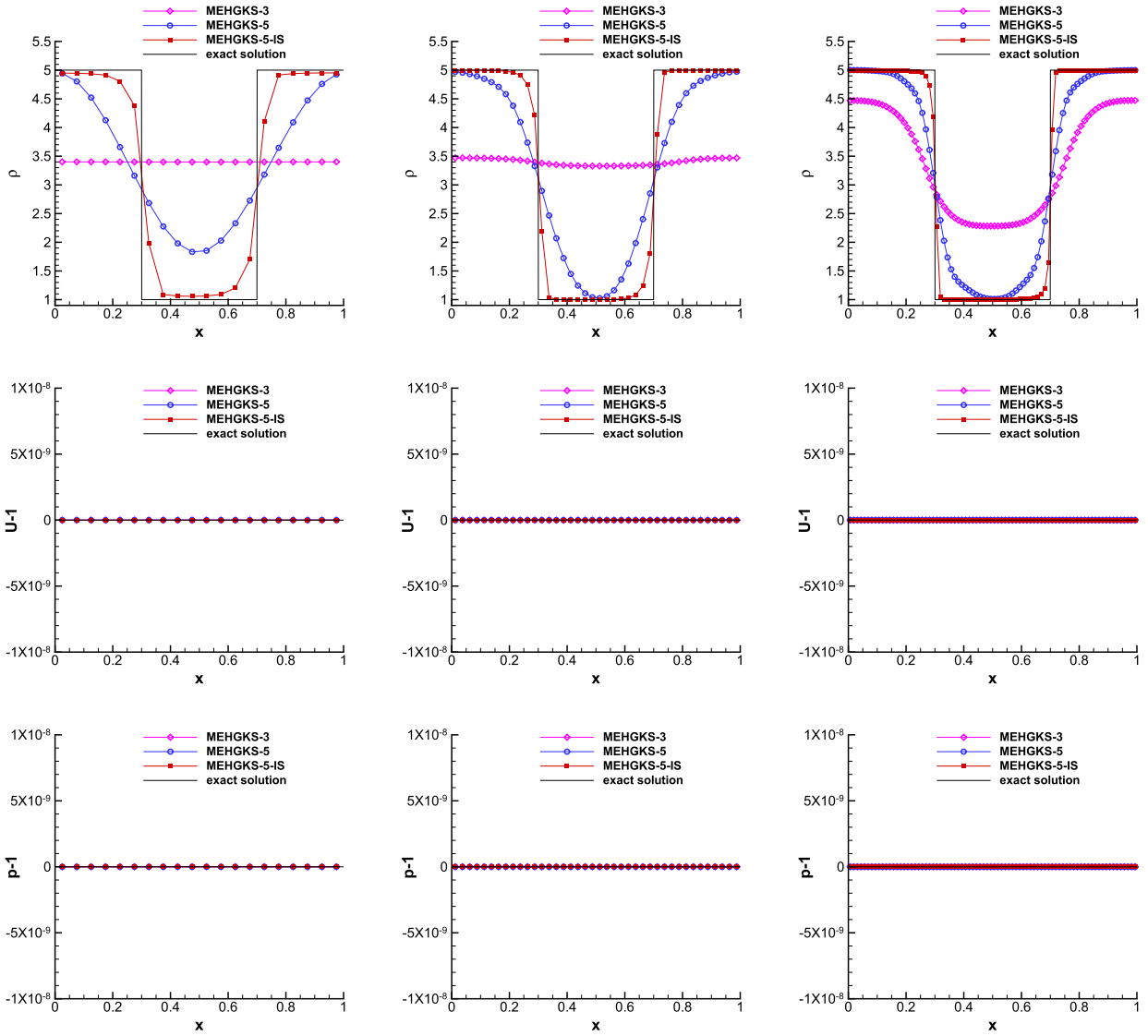


Fig. 2.  $\rho$ ,  $U$  and  $p$  of the square wave propagation problem with 20 (left), 40 (middle) and 80 (right) uniform cells at  $t = 100$ .

The output time  $t = 2.4 \times 10^{-4}$ . 5000 uniform cells are used.

Fig. 4 shows the results given by MEHGKS-3, MEHGKS-5 and MEHGKS-5-IS, demonstrating the best resolution of MEHGKS-5-IS.

#### 4.6. The two-dimensional accuracy test

In this case we assess the accuracy of MEHGKS in the two-dimensional smooth linear advection of density perturbation. The initial conditions are given by

$$(\rho, U, V, p) = (1 + 0.2 \sin(x + y), 0.7, 0.3, 1).$$

We take  $\gamma = 1.4$ ,  $p_\infty = 1$ . The corresponding analytic solutions are

$$(\rho, U, V, p) = (1 + 0.2 \sin(x + y - t), 0.7, 0.3, 1).$$

The computational domain is  $[0, 2\pi] \times [0, 2\pi]$  divided by  $N \times N$  uniform cells. The output time  $t = 2\pi$ . To test the accuracy in both space and time,  $CFL = 0.9$  in this case.

The results of the errors and the accuracy order given by MEHGKS-3 and MEHGKS-5 are shown in Table 2, from which we see that the MEHGKS scheme can achieve the designed order of accuracy in both space and time in the two-dimensional case.

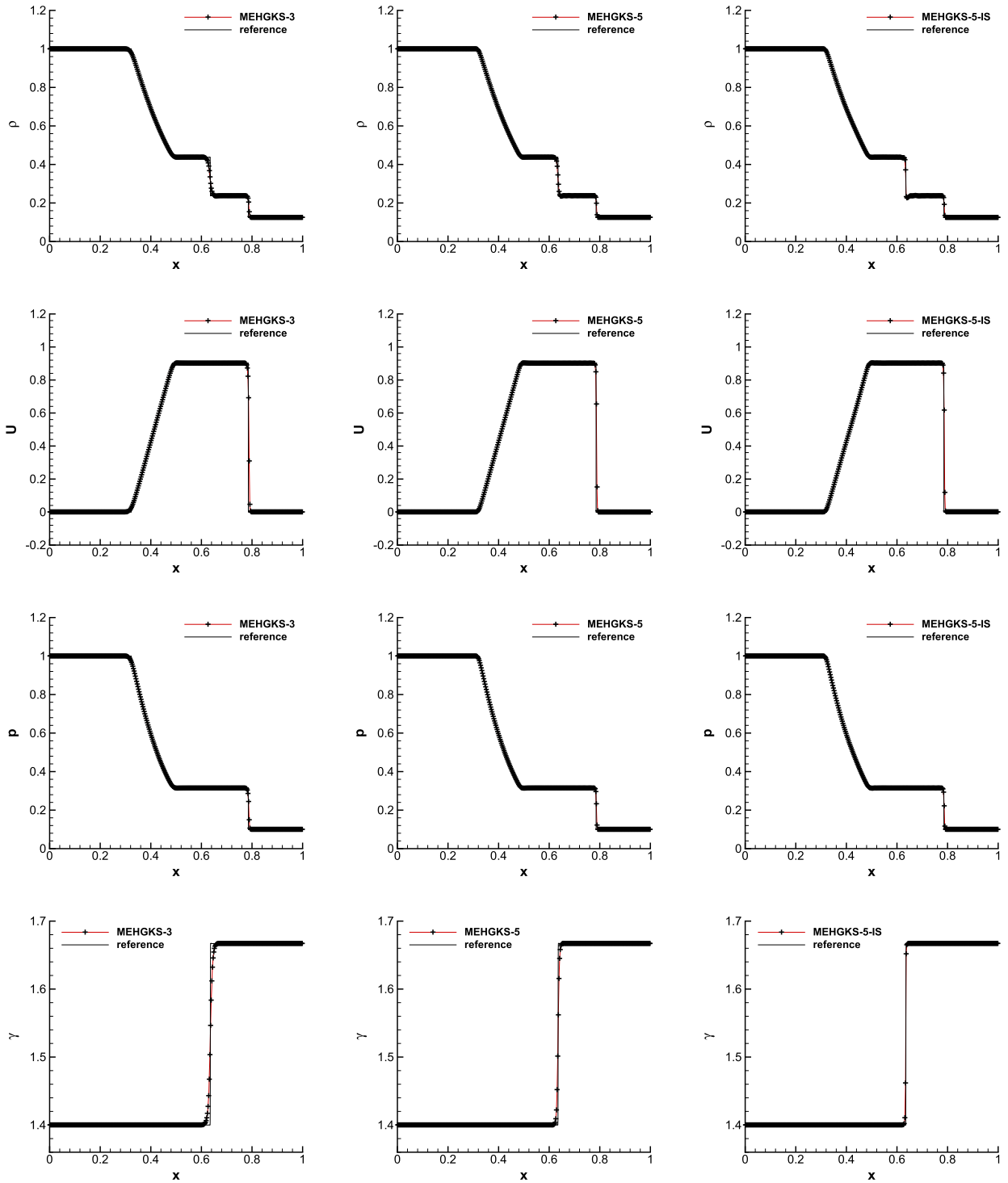


Fig. 3.  $\rho$ ,  $U$ ,  $p$  and  $\gamma$  of the gas-helium shock tube problem with 400 uniform cells at  $t = 0.15$ .

#### 4.7. The two-dimensional square wave propagating problem

Here we assess the resolution of MEHGKS in the square wave propagation [59]. The initial conditions are given by

$$(\rho, U, V, p, \gamma, p_\infty) = \begin{cases} (1, 1, 1, 1, 1.4, 1), & 0.3 < x < 0.7 \cap 0.3 < y < 0.7, \\ (0.125, 1, 1, 1, 1.9, 0), & \text{else.} \end{cases}$$

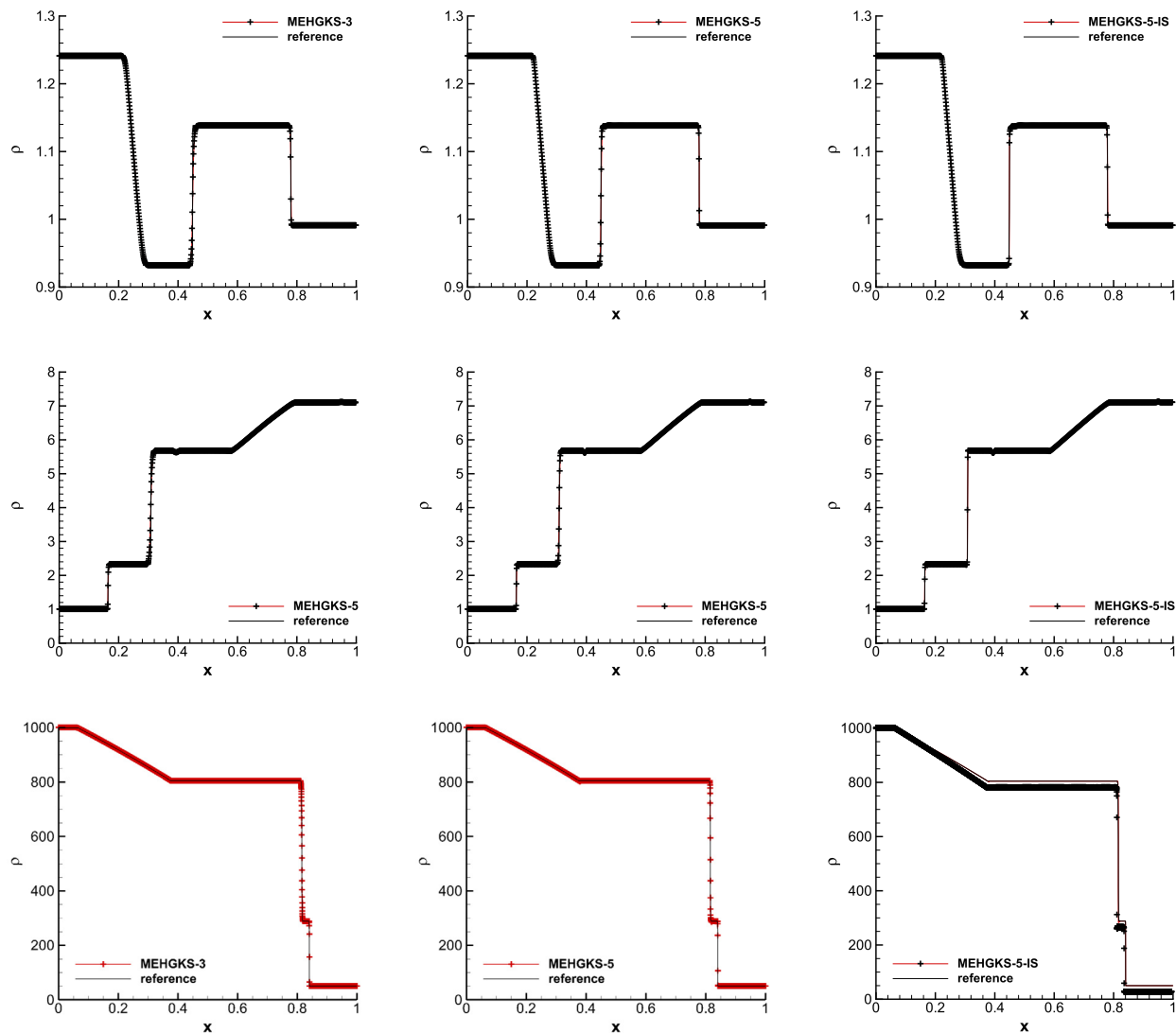


Fig. 4.  $\rho$  of the first (top), second (middle) and third (bottom) gas-liquid shock tube problems.

Table 2

Accuracy test for MEHGKS in the two-dimensional advection of density perturbation.

MEHGKS-3						
$N$	$L_1$ error	Order	$L_2$ error	Order	$L_\infty$ error	Order
10	2.62E-02		2.99E-02		4.09E-02	
20	3.98E-03	2.72	4.43E-03	2.76	6.68E-03	2.61
40	5.13E-04	2.96	5.71E-04	2.96	8.79E-04	2.93
80	6.44E-05	2.99	7.18E-05	2.99	1.11E-04	2.99
MEHGKS-5						
$N$	$L_1$ error	Order	$L_2$ error	Order	$L_\infty$ error	Order
10	2.25E-03		2.55E-03		3.58E-03	
20	7.89E-05	4.83	8.77E-05	4.86	1.35E-04	4.73
40	2.52E-06	4.97	2.80E-06	4.97	4.34E-06	4.96
80	7.89E-08	4.99	8.80E-08	4.99	1.36E-07	4.99



Fig. 5. The contours of  $\rho$  of the two-dimensional square wave propagating problem with  $80 \times 80$  cells at  $t = 4$ .

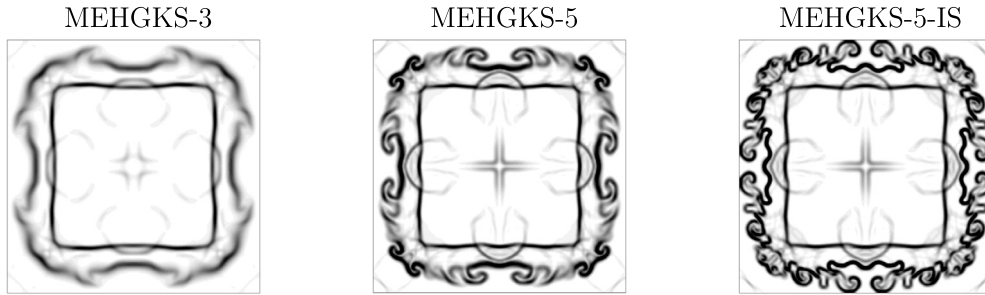


Fig. 6. The schlieren-type images of  $\rho$  of the two-dimensional sod problem with  $200 \times 200$  cells at  $t = 2$ .

The computational domain is  $[0, 1] \times [0, 1]$ .  $80 \times 80$  uniform cells are used. The periodic boundary conditions are applied on all sides of the domain.  $80 \times 80$  uniform cells are adopted.

The density distributions at  $t = 4$  are shown in Fig. 5. The interface is observed with better resolution by MEHGKS-5 than by MEHGKS-3, and by MEHGKS-5-IS than by MEHGKS-5. Fig. 5 demonstrates the advantage of high-accuracy and high-resolution scheme in simulating multi-component flows.

#### 4.8. The two-dimensional sod problem

For this problem, the initial conditions are given by

$$(\rho, U, V, p, \gamma, p_\infty) = \begin{cases} (1, 0, 0, 1, 1.4, 0), & (x - 0.5)^2 \leq 0.3^2, \\ (0.125, 0, 0, 0.1, 1.9, 0), & \text{else.} \end{cases}$$

The computational domain is  $[0, 1] \times [0, 1]$ . The reflecting boundary conditions are imposed on all sides of the domain.  $200 \times 200$  uniform cells are adopted.

The schlieren-type images of the density at  $t = 2$  are shown in Fig. 6, which confirm the best resolution of MEHGKS-5-IS.

#### 4.9. The triple point problem

The initial conditions are [59]

$$(\rho, U, V, p, \gamma, p_\infty) = \begin{cases} (1, 0, 0, 1, 1.5, 0), & x \leq 1, \\ (1, 0, 0, 0.1, 1.4, 0), & x > 1 \cap y < 1.5, \\ (0.125, 0, 0, 0.1, 1.5, 0), & \text{else.} \end{cases}$$

The computational domain is  $[0, 7] \times [0, 3]$ . The reflecting boundary conditions are imposed on the top and bottom of the domain. The non-reflecting boundary conditions are used on the left and right sides.  $840 \times 360$  uniform cells are adopted.

The schlieren-type of density at  $t = 2.4$  and  $t = 5$  are shown in Fig. 7, from which it is observed that the flow details are better captured by MEHGKS-5 than by MEHGKS-3, and further better resolved by MEHGKS-5-IS than by MEHGKS-5.

#### 4.10. The shock-bubble interaction problem

This case contains the interaction of a shock wave in air with a circular R22 bubble [58,20]. It starts from a leftward-moving shock wave with Mach 1.22 in air located at  $x = 0.25$ . In front of the shock, there is a R22 bubble with radius 0.025 centered at  $(0.225, 0)$  in water. Air is given by  $(\rho, U, V, p, \gamma, p_\infty) = (1.225, 0, 0, 1.01325 \times 10^5, 1.4, 0)$  in the pre-shock and  $(\rho, U, V, p, \gamma, p_\infty) = (1.686, -113.5, 0, 1.59 \times 10^5, 1.4, 0)$  in the post-shock regions. R22 inside the bubble is



Fig. 7. The schlieren-type images of  $\rho$  of the triple point problem with  $840 \times 360$  cells at  $t = 2.4$  (top) and  $t = 5$  (bottom).

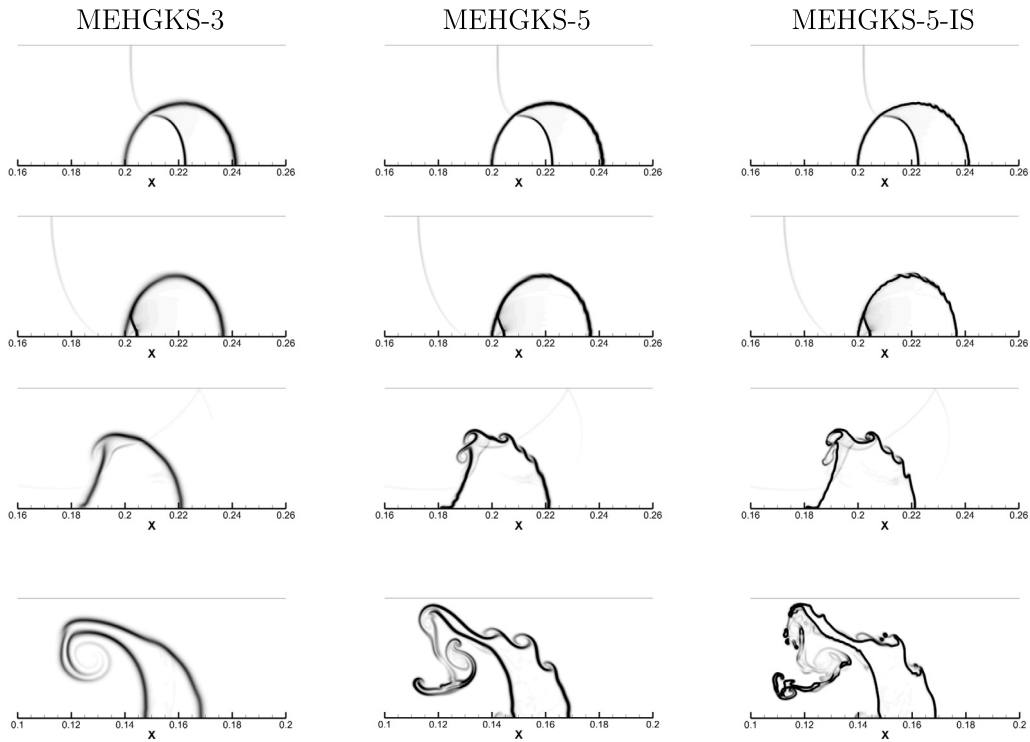


Fig. 8. The schlieren-type images of  $\rho$  of the shock-bubble interaction problem with  $1780 \times 178$  cells at  $t = (115, 187, 417, 1020) \times 10^{-6}$  (from top to bottom).

$(\rho, U, V, p, \gamma, p_\infty) = (3.863, 0, 0, 1.01325 \times 10^5, 1.249, 1)$ . The computational domain is  $[0, 0.445] \times [0, 0.0445]$ . The reflecting boundary conditions are imposed on the top and bottom of the domain. The non-reflecting boundary conditions are used on the left sides. The flows are inner flows on the right side.  $1780 \times 178$  uniform cells are adopted.

The schlieren-type images of the density are shown in Fig. 8, which demonstrate the advantage of high-accuracy scheme in capturing the flow details and high-resolution scheme in resolving the interface.

#### 4.11. Richtmyer-Meshkov instability problem

In this case, the interface between air and liquid is initially generated at  $x = 1.2 + 0.1 \cos(2\pi y) = f(y)$  [56,38]. The initial conditions are

$$(\rho, U, V, p, \gamma, p_\infty) = \begin{cases} (1, 0, 0, 1, 1.4, 0), & x \leq f(y), \\ (5, 0, 0, 1, 4, 1), & x \leq 1.325, \\ (7.093, -0.7288, 0, 10, 4, 1), & \text{else.} \end{cases}$$

The computational domain is  $[-2, 2] \times [0, 0.5]$ . The reflecting boundary conditions are imposed on the top and bottom of the domain. The non-reflecting boundary conditions are used on the left sides. The flows are inner flows on the right side.  $2560 \times 320$  uniform cells are adopted.

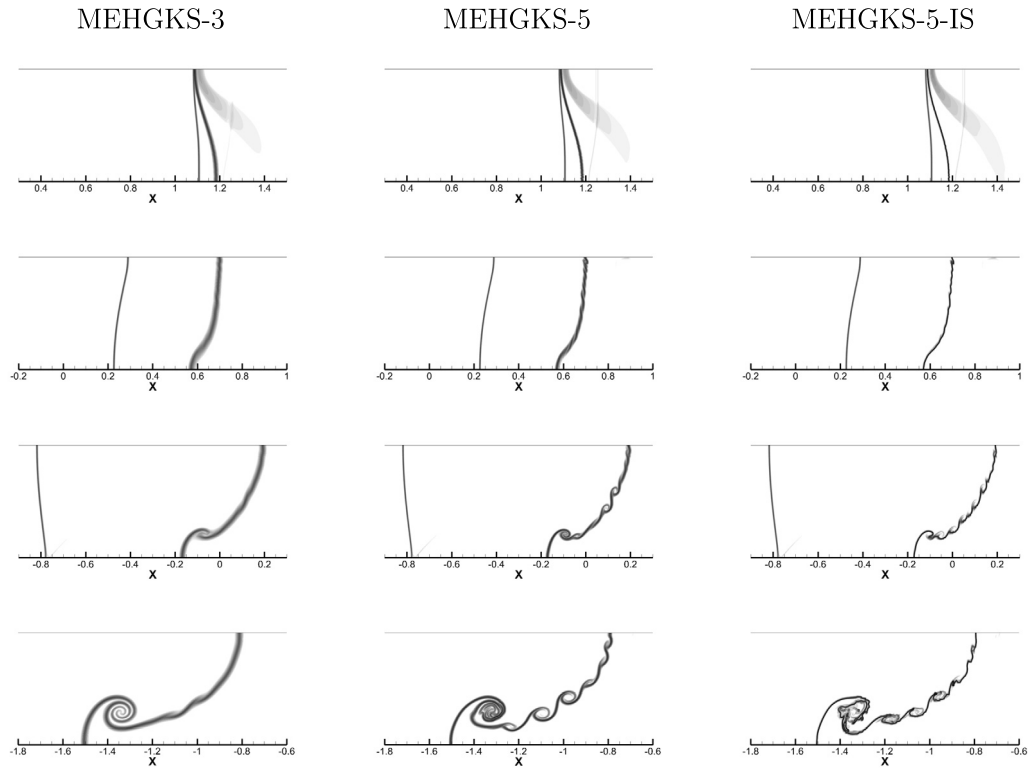


**Fig. 9.** The schlieren-type images of  $\rho$  of the Richtmyer-Meshkov instability problem with  $2560 \times 320$  cells at  $t = 0.1, 0.5, 1, 2$  (from top to bottom).

The schlieren-type images of the density are shown in Fig. 9. The oscillations are captured by MEHGKS-5 and MEHGKS-5-IS. The interface is better resolved by MEHGKS-5-IS than by MEHGKS-5.

#### 4.12. Underwater explosion problem

This case has been extensively adopted to test the performance of numerical schemes in media with large variations of the pressure and density [58,19]. Initially, a stationary interface between air and water is located at  $y = 0$ . Air is given by  $(\rho, p, \gamma, p_\infty) = (1.225, 1.01325 \times 10^5, 1.4, 0)$ . Water is  $(\rho, p, \gamma, p_\infty) = (10^3, 1.01325 \times 10^5, 4.4, 6 \times 10^8)$ . There is a bubble with air  $(\rho, p, \gamma, p_\infty) = (1250, 10^9, 1.4, 0)$  centering at  $(0, -0.3)$  in water. Its radius is 0.12. The computational domain is  $[0, 2] \times [-1.5, 1]$ . The reflecting boundary conditions are imposed on the bottom and left sides of the domain. The non-reflecting boundary conditions are used on the remaining sides.  $400 \times 500$  uniform cells are adopted.

The schlieren-type images of the density and pressure are shown in Figs. 10-11. The interface is better resolved by MEHGKS-5 than by MEHGKS-3, which demonstrates the advantage of a high-accuracy scheme in the simulations of multi-component flows. It also shows that the interface is better resolved by MEHGKS-5-IS than by MEHGKS-5, which demonstrates the advantage of a high-resolution scheme.

## 5. Conclusions and comments

Based on the framework of EHGKS with a newly-developed interface-sharpening technique, a one-stage high-accuracy and high-resolution scheme is proposed for inviscid compressible immiscible multi-component flows. Firstly, the original EHGKS for a single ideal gas is modified for stiffened gases based on NOK. Secondly, the scheme is extended under Abgrall's 4-equations model to solve the non-conservative parts of model with no spurious oscillations across material interfaces. Together with a newly-developed interface-sharpening technique, the proposed scheme possesses not only uniform high order of accuracy in both space and time in smooth regions of a pure medium, but also the high resolution on the material interfaces.

Several benchmark tests are carried out to validate the high accuracy and resolution of the proposed scheme. The designed third and fifth order of accuracy in both space and time is validated. Comparisons are made between MEHGKS-3, MEHGKS-5 and MEHGKS-IS. On the one hand, MEHGKS-5 presents more flow details than MEHGKS-3, illustrating the advantage of high accuracy. On the other hand, MEHGKS-5-IS can capture a material interface more sharply than MEHGKS-5, demonstrating the advantage of its high resolution. As a conclusion, the high accuracy and resolution of the new scheme is confirmed.

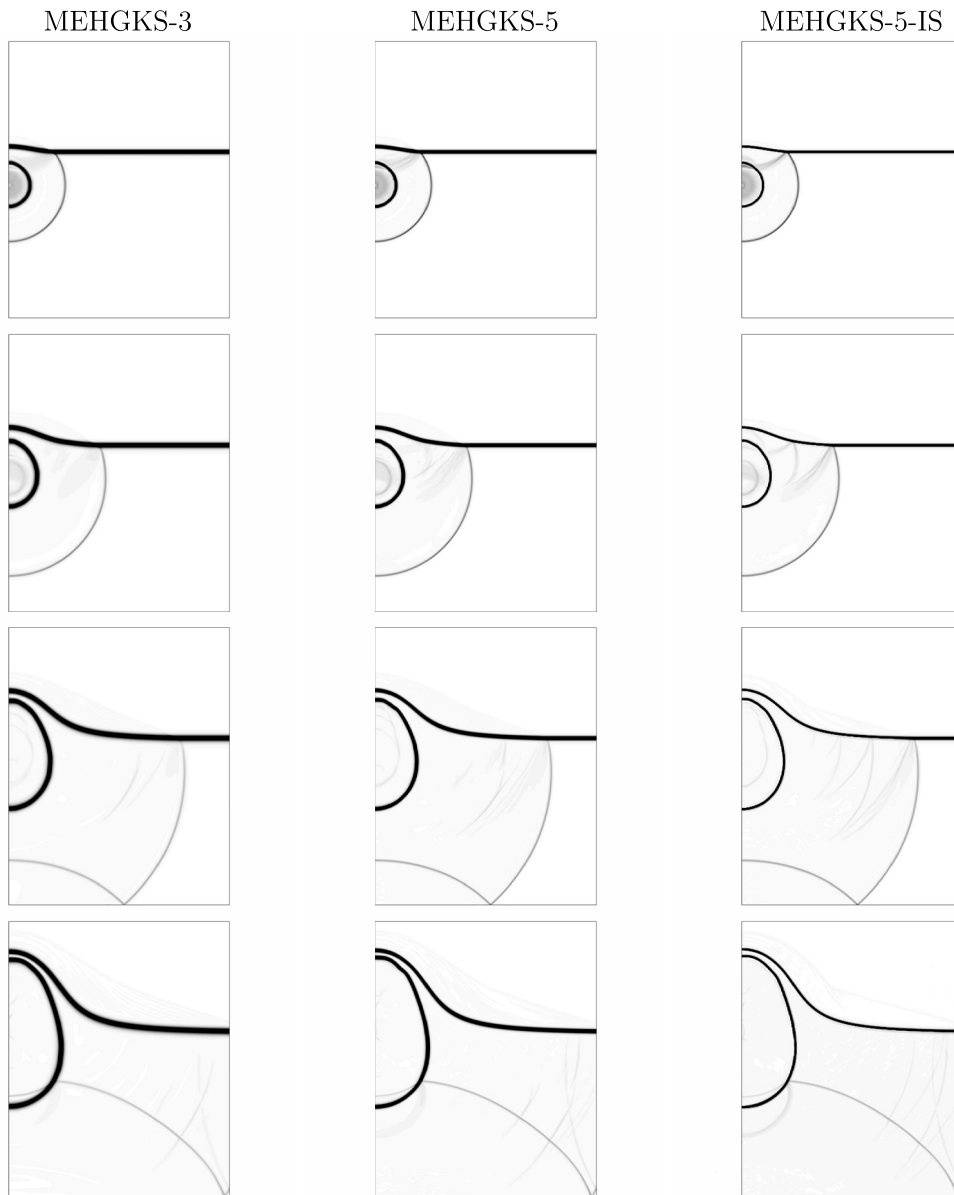


**Fig. 10.** The schlieren-type images of  $\rho$  of the underwater explosion problem with  $400 \times 500$  cells at  $t = 2 \times 10^{-4}, 4 \times 10^{-3}, 8 \times 10^{-3}$  and  $1.2 \times 10^{-3}$  (from top to bottom).

The new method is developed for the stiffened gases in this work. It is also possible to extend it to a more general equation of state. In fact, NOK, which builds up the leading terms in flux and source evaluations of MEHGKS, has already been extended to the Mie-Grüneisen equation of state [40]. The key then should be on the modification of the Lax-Wendroff procedure to obtain the high-order terms in flux evaluations. We will continue this work in the future.

#### Declaration of competing interest

The authors declare that they have no known competing financial interests or personal relationships that could have appeared to influence the work reported in this paper.

#### Data availability

Data will be made available on request.



Fig. 11. The schlieren-type images of  $p$  of the underwater explosion problem with  $400 \times 500$  cells at  $t = 2 \times 10^{-4}, 4 \times 10^{-3}, 8 \times 10^{-3}$  and  $1.2 \times 10^{-3}$  (from top to bottom).

**Acknowledgements**

This work is supported by National Key R&D Program of China (Grant Nos. 2022YFA1004500, 2020YFA0712200), NSFC (Grant Nos. 11901044, 12271052, 12101063, 12071392), National Key Project (Grant No. GJXM92579), the Sino-German Science Center (Grant No. GZ 1465) and ISF-NSFC joint research program (Grant No. 11761141008).

**Appendix A. Reconstruction**

The traditional WENO reconstruction technique [27] is applied to obtain the point-wise values at a cell interface. The definitions of  $\mathbf{W}_{i+\frac{1}{2}^\pm}$  are

$$\mathbf{W}_{i+\frac{1}{2}^-} = \lim_{x \rightarrow x_{i+\frac{1}{2}}} \mathbf{W}(x, 0), x \in \left[ x_{i-\frac{1}{2}}, x_{i+\frac{1}{2}} \right),$$

$$\mathbf{W}_{i+\frac{1}{2}^+} = \lim_{x \rightarrow x_{i+\frac{1}{2}}} \mathbf{W}(x, 0), x \in \left[ x_{i+\frac{1}{2}}, x_{i+\frac{3}{2}} \right].$$

To guarantee  $U_{i+\frac{1}{2}^\pm} = U_0$  and  $p_{i+\frac{1}{2}^\pm} = p_0$  under the condition  $\bar{U}_i^n = U_0$  and  $\bar{p}_i^n = p_0$  for  $i = 1, 2, \dots, N$ , the WENO reconstruction is implemented on  $(\bar{p}_i^n, \bar{U}_i^n, \bar{p}_i^n, \bar{V}_i^n)$ . In this section, we define  $\mathbf{Q} = (\rho, U, p, Y)$  for simplicity.

To evaluate the spatial derivatives of  $\mathbf{Q}^e$ , the linear reconstruction is implemented based on the point-wise values  $\mathbf{Q}^e$  and the centremost cell averages  $\bar{\mathbf{Q}}_i^n, \bar{\mathbf{Q}}_{i+1}^n, \dots$ , i.e., in the third-order scheme,

$$\begin{aligned} \frac{\partial \mathbf{Q}^e}{\partial x} &= \frac{1}{\Delta x} (\bar{\mathbf{Q}}_{i+1}^n - \bar{\mathbf{Q}}_i^n), \\ \frac{\partial^2 \mathbf{Q}^e}{\partial x^2} &= \frac{1}{\Delta x^2} (3\bar{\mathbf{Q}}_i^n - 6\mathbf{Q}^e + 3\bar{\mathbf{Q}}_{i+1}^n); \end{aligned}$$

in the fifth-order scheme,

$$\begin{aligned} \frac{\partial \mathbf{Q}^e}{\partial x} &= \frac{1}{12\Delta x} (\bar{\mathbf{Q}}_{i-1}^n - 15\bar{\mathbf{Q}}_i^n + 15\bar{\mathbf{Q}}_{i+1}^n - \bar{\mathbf{Q}}_{i+2}^n), \\ \frac{\partial^2 \mathbf{Q}^e}{\partial x^2} &= \frac{1}{8\Delta x^2} (-\bar{\mathbf{Q}}_{i-1}^n + 31\bar{\mathbf{Q}}_i^n - 60\mathbf{Q}^e + 31\bar{\mathbf{Q}}_{i+1}^n - \bar{\mathbf{Q}}_{i+2}^n), \\ \frac{\partial^3 \mathbf{Q}^e}{\partial x^3} &= \frac{1}{\Delta x^3} (-\bar{\mathbf{Q}}_{i-1}^n + 3\bar{\mathbf{Q}}_i^n - 3\bar{\mathbf{Q}}_{i+1}^n + \bar{\mathbf{Q}}_{i+2}^n), \\ \frac{\partial^4 \mathbf{Q}^e}{\partial x^4} &= \frac{1}{2\Delta x^4} (5\bar{\mathbf{Q}}_{i-1}^n - 35\bar{\mathbf{Q}}_i^n + 60\mathbf{Q}^e - 35\bar{\mathbf{Q}}_{i+1}^n + 5\bar{\mathbf{Q}}_{i+2}^n). \end{aligned}$$

In the two-dimensional case, the reconstruction is implemented dimension-by-dimension. The tangential derivatives of  $\mathbf{Q}^e$  are evaluated by the linear reconstruction based on  $\frac{\partial^m \mathbf{Q}^e}{\partial x^m}$  in the centers of the tangential faces. The subscript  $j$  is added to indicate the  $j$ -th face in the tangential direction. In the third-order scheme,

$$\begin{aligned} \frac{\partial^{m+1} \mathbf{Q}_j^e}{\partial y \partial x^m} &= \frac{1}{2\Delta y} \left( \frac{\partial^m \mathbf{Q}_{j+1}^e}{\partial x^m} - \frac{\partial^m \mathbf{Q}_{j-1}^e}{\partial x^m} \right), \\ \frac{\partial^{m+2} \mathbf{Q}_j^e}{\partial y^2 \partial x^m} &= \frac{1}{\Delta y^2} \left( \frac{\partial^m \mathbf{Q}_{j-1}^e}{\partial x^m} - 2 \frac{\partial^m \mathbf{Q}_j^e}{\partial x^m} + \frac{\partial^m \mathbf{Q}_{j+1}^e}{\partial x^m} \right). \end{aligned}$$

In the fifth-order scheme,

$$\begin{aligned} \frac{\partial^{m+1} \mathbf{Q}_j^e}{\partial y \partial x^m} &= \frac{1}{12\Delta y} \left( -\frac{\partial^m \mathbf{Q}_{j-2}^e}{\partial x^m} + 8 \frac{\partial^m \mathbf{Q}_{j-1}^e}{\partial x^m} - 8 \frac{\partial^m \mathbf{Q}_{j+1}^e}{\partial x^m} + \frac{\partial^m \mathbf{Q}_{j+2}^e}{\partial x^m} \right), \\ \frac{\partial^{m+2} \mathbf{Q}_j^e}{\partial y^2 \partial x^m} &= \frac{1}{12\Delta y^2} \left( \frac{\partial^m \mathbf{Q}_{j-2}^e}{\partial x^m} - 16 \frac{\partial^m \mathbf{Q}_{j-1}^e}{\partial x^m} + 30 \frac{\partial^m \mathbf{Q}_j^e}{\partial x^m} - 16 \frac{\partial^m \mathbf{Q}_{j+1}^e}{\partial x^m} + \frac{\partial^m \mathbf{Q}_{j+2}^e}{\partial x^m} \right), \\ \frac{\partial^{m+3} \mathbf{Q}_j^e}{\partial y^3 \partial x^m} &= \frac{1}{2\Delta y^3} \left( -\frac{\partial^m \mathbf{Q}_{j-2}^e}{\partial x^m} + 2 \frac{\partial^m \mathbf{Q}_{j-1}^e}{\partial x^m} - 2 \frac{\partial^m \mathbf{Q}_{j+1}^e}{\partial x^m} + \frac{\partial^m \mathbf{Q}_{j+2}^e}{\partial x^m} \right), \\ \frac{\partial^{m+4} \mathbf{Q}_j^e}{\partial y^4 \partial x^m} &= \frac{1}{\Delta y^4} \left( \frac{\partial^m \mathbf{Q}_{j-2}^e}{\partial x^m} - 4 \frac{\partial^m \mathbf{Q}_{j-1}^e}{\partial x^m} + 6 \frac{\partial^m \mathbf{Q}_j^e}{\partial x^m} - 4 \frac{\partial^m \mathbf{Q}_{j+1}^e}{\partial x^m} + \frac{\partial^m \mathbf{Q}_{j+2}^e}{\partial x^m} \right). \end{aligned}$$

**Remark 4.** The present reconstruction can not preserve the inherent positivity of the density and pressure.  $Y$  is also not ensured between the range  $[0, 1]$ . For simplicity, all the reconstruction and flux evaluations are reduced to the first order of accuracy when the reconstructed point-wise density is negative, or the speed of sound is not real, or  $Y_{i+\frac{1}{2}^\pm} < -\epsilon$  or  $Y_{i+\frac{1}{2}^\pm} > 1 + \epsilon$ . The work to develop a positivity-preserving and border-preserving one-stage high-order method [72] will be studied in the future.

**Appendix B. The proof of Eq. (18) for MEHGKS**

Lemma. Assume Eq. (17), Eq. (18) is satisfied by MEHGKS with the reconstruction, flux and source evaluations defined in Appendix A, Eq. (16) and Eq. (24).

Proof. The initial condition is given by Eq. (17). Based on the reconstruction in Appendix A, we have

$$\begin{aligned} U_{i+\frac{1}{2}^\pm} &= U_0, \\ p_{i+\frac{1}{2}^\pm} &= p_0. \end{aligned} \tag{B.1}$$

And given by the definition of  $\mathbb{Q}^{e,\text{NOK}}$  in Eq. (13), we have

$$\begin{aligned} U^{e,\text{NOK}} &= U_0, \\ p^{e,\text{NOK}} &= p_0, \\ \frac{\partial^m U^{e,\text{NOK}}}{\partial x^m} &= 0, \\ \frac{\partial^m p^{e,\text{NOK}}}{\partial x^m} &= 0, \end{aligned} \tag{B.2}$$

for  $m = 1, 2, \dots, r$ . The equation of state gives

$$\begin{aligned} \frac{1}{\gamma^{e,\text{NOK}} - 1} &= \frac{1}{\gamma^{(1)} - 1} Y^{e,\text{NOK}} + \frac{1}{\gamma^{(2)} - 1} (1 - Y^{e,\text{NOK}}), \\ \frac{\gamma^{e,\text{NOK}} p_\infty^{e,\text{NOK}}}{\gamma^{e,\text{NOK}} - 1} &= \frac{\gamma^{(1)} p_\infty^{(1)}}{\gamma^{(1)} - 1} Y^{e,\text{NOK}} + \frac{\gamma^{(2)} p_\infty^{(2)}}{\gamma^{(2)} - 1} (1 - Y^{e,\text{NOK}}). \end{aligned} \tag{B.3}$$

Substituting Eqs. (B.2)-(B.3) into  $\mathbb{F}^{e,\text{NOK}}$  results in

$$\mathbb{F}^{e,\text{NOK}} = \begin{pmatrix} \rho^{e,\text{NOK}} U_0 \\ \rho^{e,\text{NOK}} U_0^2 + p_0 \\ \frac{1}{2} \rho^{e,\text{NOK}} U_0^3 + C_0 Y^{e,\text{NOK}} U_0 + p_0 U_0 + \frac{p_0 + \gamma^{(2)} p_\infty^{(2)}}{\gamma^{(2)} - 1} U_0 \end{pmatrix}, \tag{B.4}$$

where  $C_0 = \frac{p_0 + \gamma^{(1)} p_\infty^{(1)}}{\gamma^{(1)} - 1} - \frac{p_0 + \gamma^{(2)} p_\infty^{(2)}}{\gamma^{(2)} - 1}$ . The temporal derivatives of  $\mathbb{F}^{e,\text{NOK}}$  can be obtained by the spatial derivatives according to the Lax-Wendroff procedure in Eq. (25), which gives

$$\frac{\partial^{m+l}}{\partial x^m \partial t^l} \left( \frac{\partial U^{e,\text{NOK}}}{\partial t} + U^{e,\text{NOK}} \frac{\partial U^{e,\text{NOK}}}{\partial x} + \frac{1}{\rho^{e,\text{NOK}}} \frac{\partial p^{e,\text{NOK}}}{\partial x} \right) = 0,$$

and

$$\frac{\partial^{m+l}}{\partial x^m \partial t^l} \left( \frac{\partial p^{e,\text{NOK}}}{\partial t} + \gamma^{e,\text{NOK}} (p^{e,\text{NOK}} + p_\infty^{e,\text{NOK}}) \frac{\partial U^{e,\text{NOK}}}{\partial x} + U^{e,\text{NOK}} \frac{\partial p^{e,\text{NOK}}}{\partial x} \right) = 0,$$

for  $m + l = 0, 1, \dots, r - 1$ . Since the reconstruction results in Eq. (B.2), we then have

$$m = 0, l = 0 : \frac{\partial U^{e,\text{NOK}}}{\partial t} = 0, \frac{\partial p^{e,\text{NOK}}}{\partial t} = 0;$$

and subsequently

$$\begin{aligned} m = 1, l = 0 : \frac{\partial^2 U^{e,\text{NOK}}}{\partial x \partial t} &= 0, \frac{\partial^2 p^{e,\text{NOK}}}{\partial x \partial t} = 0; \\ m = 0, l = 1 : \frac{\partial^2 U^{e,\text{NOK}}}{\partial t^2} &= 0, \frac{\partial^2 p^{e,\text{NOK}}}{\partial t^2} = 0; \\ &\dots, \dots; \\ &\dots, \dots; \\ m = 0, l = r - 1 : \frac{\partial^r U^{e,\text{NOK}}}{\partial t^r} &= 0, \frac{\partial^r p^{e,\text{NOK}}}{\partial t^r} = 0. \end{aligned}$$

As a result,

$$\frac{\partial^l \mathbb{F}^{e,\text{NOK}}}{\partial t^l} = U_0 \frac{\partial^l}{\partial t^l} \begin{pmatrix} \rho^{e,\text{NOK}} \\ \rho^{e,\text{NOK}} U_0 \\ \frac{1}{2} \rho^{e,\text{NOK}} U_0^2 + C_0 Y^{e,\text{NOK}} \end{pmatrix}. \tag{B.5}$$

Substituting the equation of state into  $\mathbb{F}^{k,\text{NOK}}$  results in

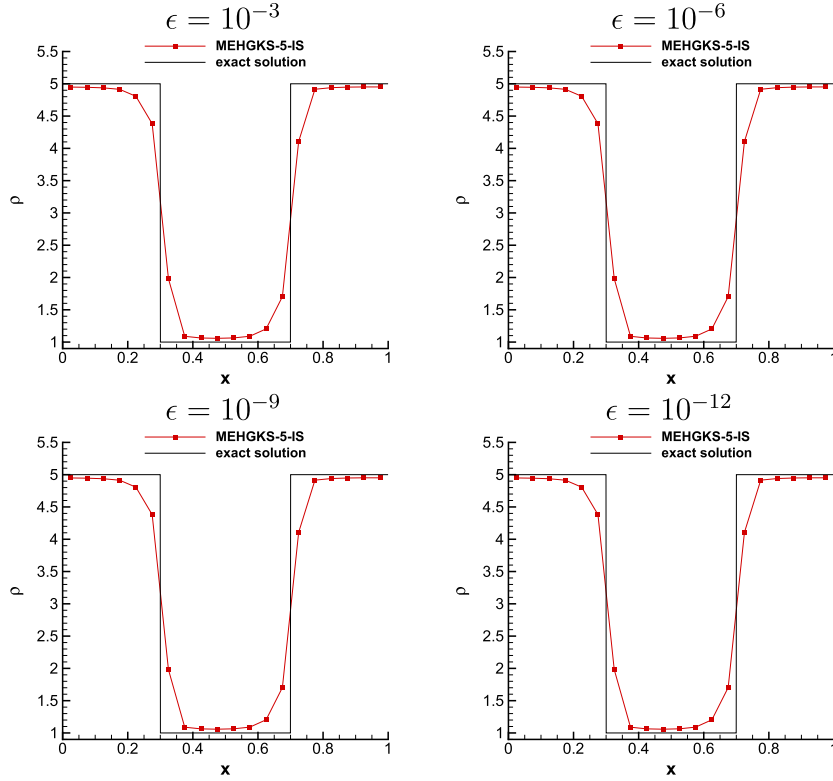


Fig. C.12.  $\rho$  of the square wave propagation problem (Section 4.3) with 20 uniform cells at  $t = 100$ .

$$\mathbb{F}^{k,\text{NOK}} = \begin{pmatrix} \mathbb{F}(1)^{k,\text{NOK}} \\ U_0 \mathbb{F}(1)^{k,\text{NOK}} + p_0 \\ \frac{1}{2} U_0^2 \mathbb{F}(1)^{k,\text{NOK}} + C_0 \mathbb{F}_Y^{k,\text{NOK}} + p_0 U_0 + \frac{p_0 + \gamma^{(2)} p_\infty^{(2)}}{\gamma^{(2)} - 1} U_0 \end{pmatrix}, \quad (\text{B.6})$$

where  $\mathbb{F}(1)^{k,\text{NOK}} = \langle u^1 \rangle^+, \text{NOK} \rho_{i+\frac{1}{2}} + \langle u^1 \rangle^-, \text{NOK} \rho_{i+\frac{1}{2}}$ . In Eq. (22),  $\mathbb{F}(3)^{k,\text{NOK}} = \frac{1}{2} U_0^2 \mathbb{F}(1)^{k,\text{NOK}} + C_0 \mathbb{F}_Y^{k,\text{NOK}} + \frac{\gamma^{(2)}}{\gamma^{(2)} - 1} (p_0 + p_\infty^{(2)}) U_0$ . Substituting Eqs. (B.5)-(B.6) back into Eqs. (2) and (10) results in Eqs. (20)-(23). Based on Eqs. (20) and (21),  $\bar{U}_i^{n+1} = U_0$  is satisfied. After substituting the equation of state into Eq. (22), Eq. (22) can be written as

$$\begin{aligned} & \frac{1}{2} \bar{\rho}_i^{n+1} U_0^2 + \left( \frac{\bar{p}_i^{n+1} + \gamma^{(1)} p_\infty^{(1)}}{\gamma^{(1)} - 1} - \frac{\bar{p}_i^{n+1} + \gamma^{(2)} p_\infty^{(2)}}{\gamma^{(2)} - 1} \right) \bar{Y}_i^{n+1} + \frac{\bar{p}_i^{n+1} + \gamma^{(2)} p_\infty^{(2)}}{\gamma^{(2)} - 1} \\ &= \frac{1}{2} \bar{\rho}_i^n U_0^2 + \left( \frac{p_0 + \gamma^{(1)} p_\infty^{(1)}}{\gamma^{(1)} - 1} - \frac{p_0 + \gamma^{(2)} p_\infty^{(2)}}{\gamma^{(2)} - 1} \right) \bar{Y}_i^n + \frac{p_0 + \gamma^{(2)} p_\infty^{(2)}}{\gamma^{(2)} - 1} \\ & - \frac{1}{2} U_0^2 \frac{\Delta t}{\Delta x} \left( \nabla \mathbb{F}(1)^{k,\text{NOK}} + U_0 \left( 1 - e^{-\frac{1}{c_1}} \right) \sum_{l=1}^r \frac{\Delta t^l}{(l+1)!} \frac{\partial^l \nabla \rho^{e,\text{NOK}}}{\partial t^l} \right) \\ & - C_0 \frac{\Delta t}{\Delta x} \left( \nabla \mathbb{F}_Y^{k,\text{NOK}} + U_0 \left( 1 - e^{-\frac{1}{c_1}} \right) \sum_{l=1}^r \frac{\Delta t^l}{(l+1)!} \frac{\partial^l}{\partial t^l} \nabla Y^{e,\text{NOK}} \right). \end{aligned} \quad (\text{B.7})$$

And substituting Eq. (20) into Eq. (B.7) results in

$$\begin{aligned} & C_0 \bar{Y}_i^{n+1} = C_0 \bar{Y}_i^n \\ & - C_0 \frac{\Delta t}{\Delta x} \left( \nabla \mathbb{F}_Y^{k,\text{NOK}} + U_0 \left( 1 - e^{-\frac{1}{c_1}} \right) \sum_{l=1}^r \frac{\Delta t^l}{(l+1)!} \frac{\partial^l}{\partial t^l} \nabla Y^{e,\text{NOK}} \right) \\ & - \left( \left( \frac{1}{\gamma^{(1)} - 1} - \frac{1}{\gamma^{(2)} - 1} \right) \bar{Y}_i^{n+1} + \frac{1}{\gamma^{(2)} - 1} \right) (\bar{p}_i^{n+1} - p_0). \end{aligned} \quad (\text{B.8})$$

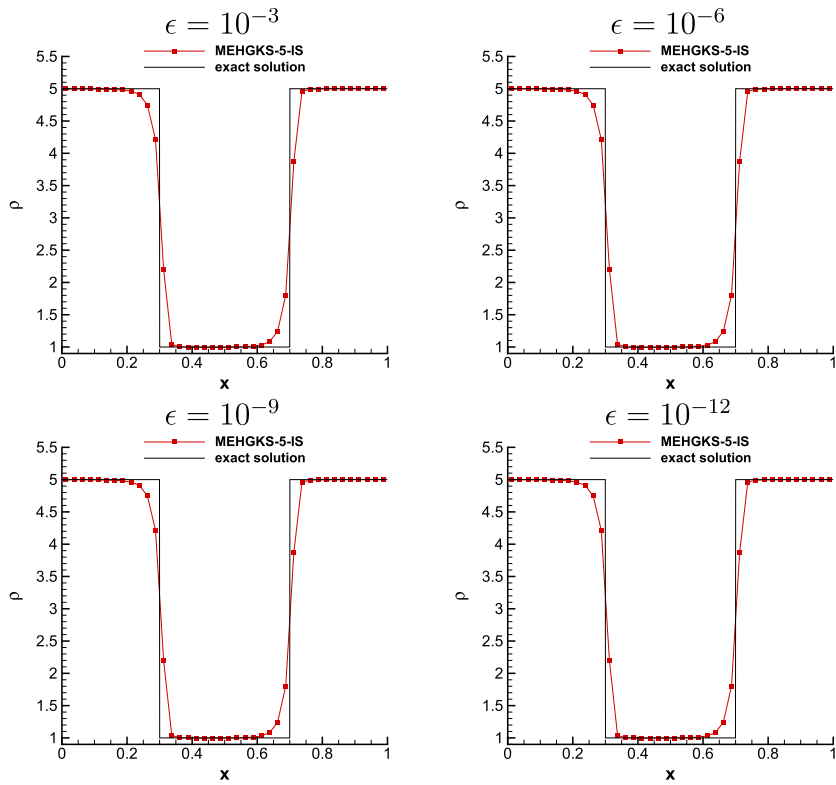


Fig. C.13.  $\rho$  of the square wave propagation problem (Section 4.3) with 40 uniform cells at  $t = 100$ .

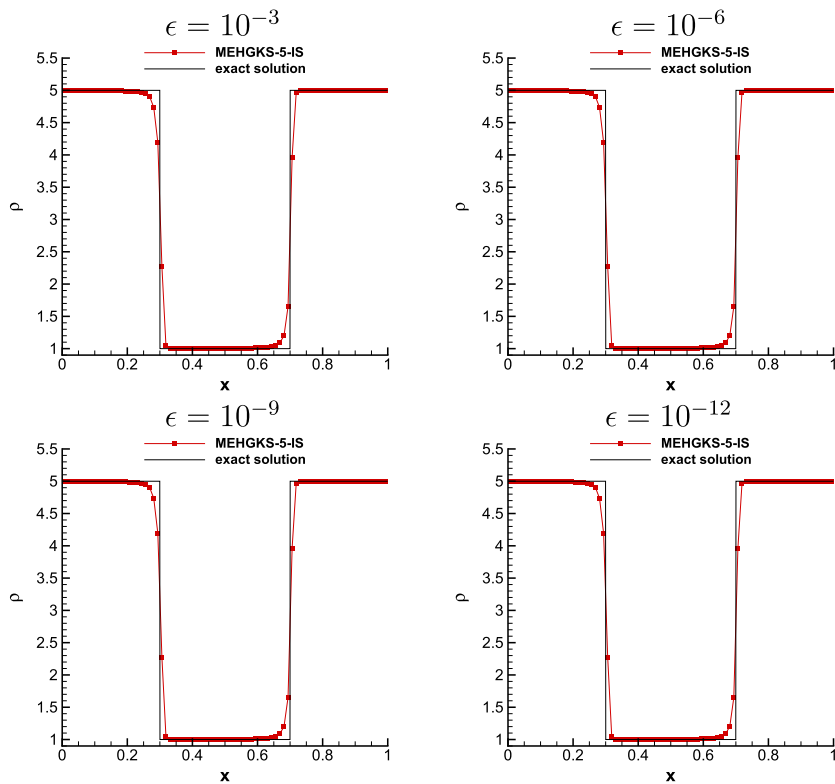


Fig. C.14.  $\rho$  of the square wave propagation problem (Section 4.3) with 80 uniform cells at  $t = 100$ .

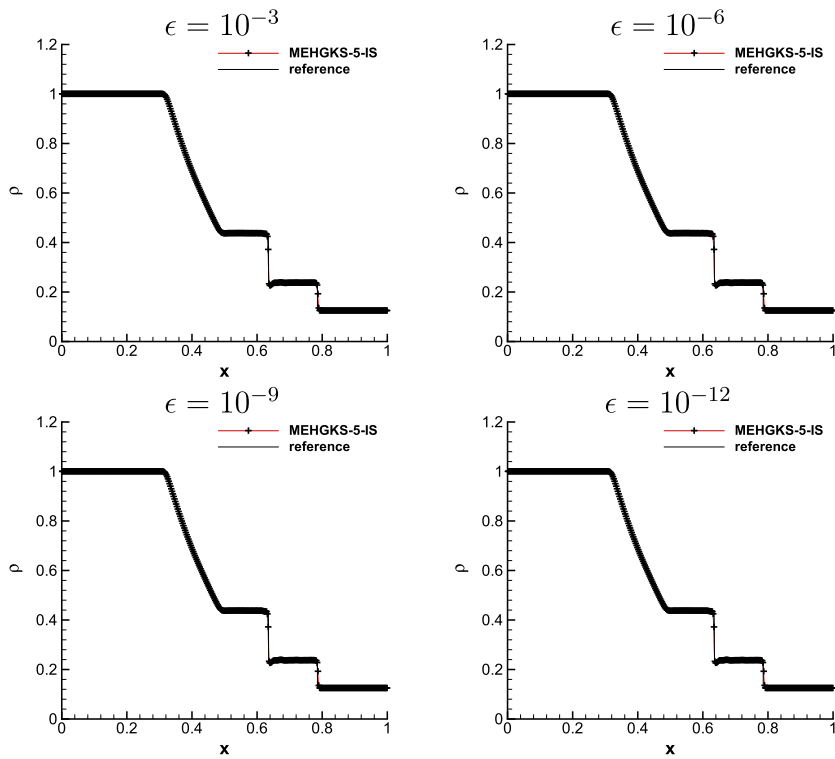


Fig. C.15.  $\rho$  of the gas-helium shock tube problem (Section 4.4) with 400 uniform cells at  $t = 0.15$ .

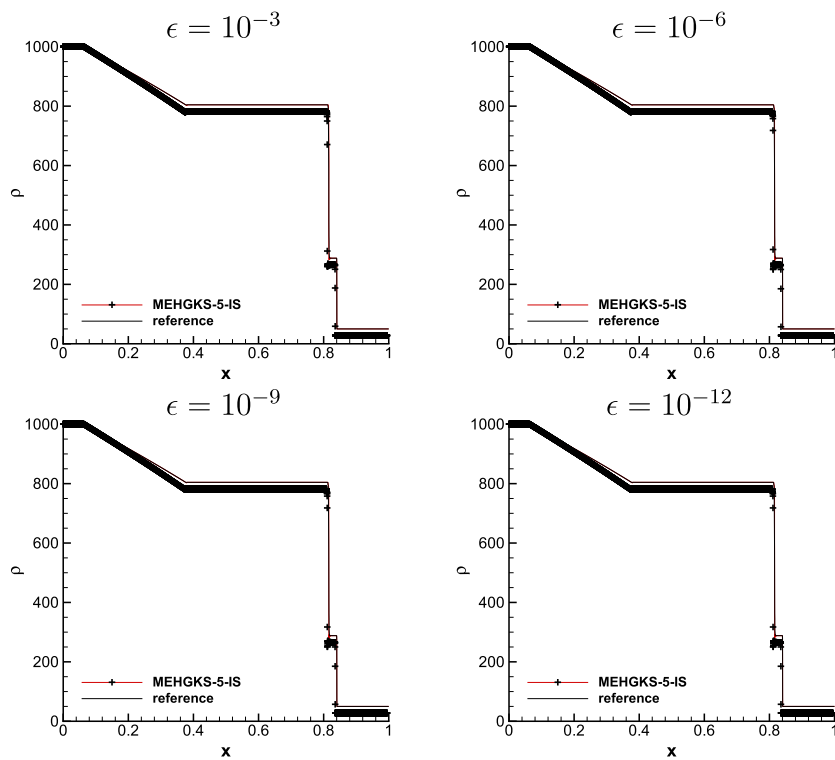


Fig. C.16.  $\rho$  of the gas-liquid shock tube problems (the third case in Section 4.5).

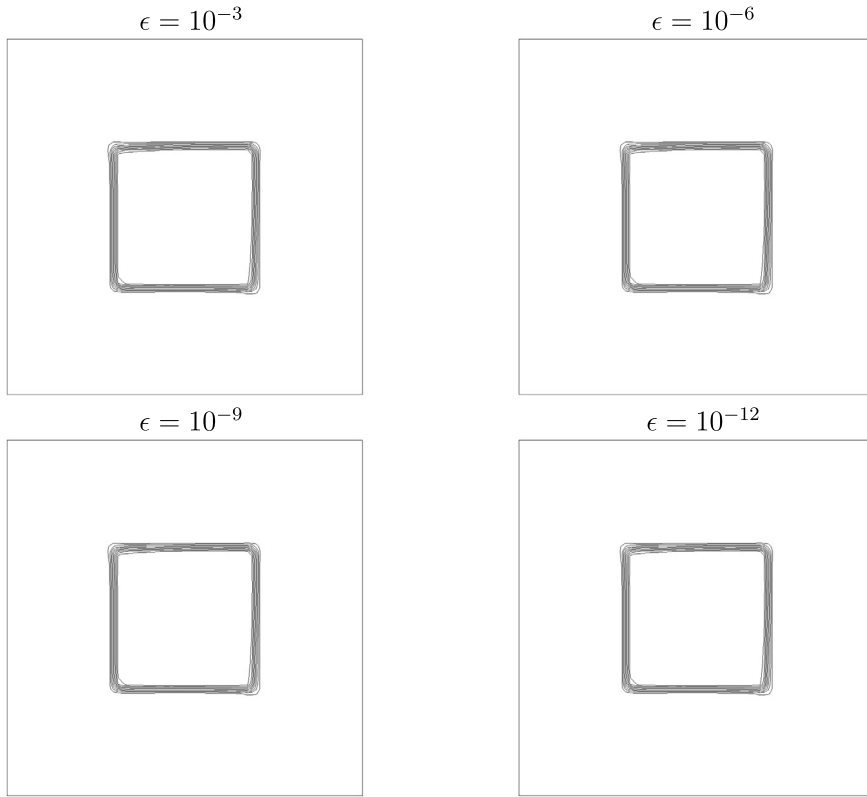


Fig. C.17. The contours of  $\rho$  of the two-dimensional square wave propagating problem (Section 4.7) with  $80 \times 80$  cells at  $t = 4$ .

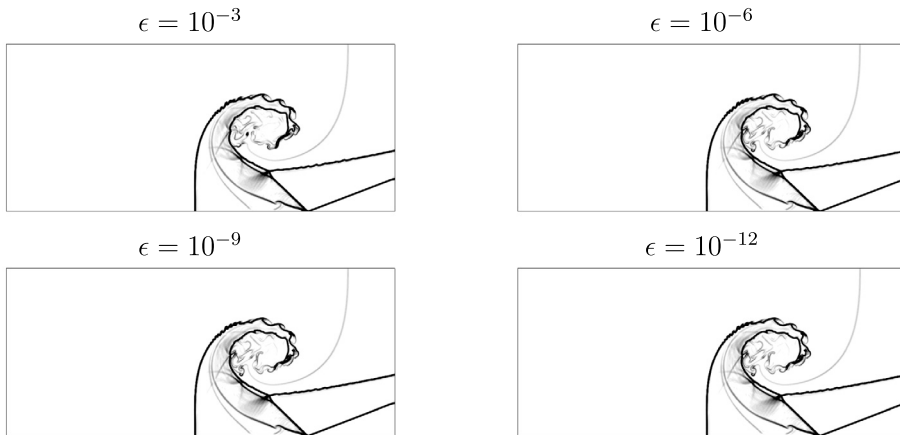


Fig. C.18. The schlieren-type images of  $\rho$  of the triple point problem (Section 4.9) with  $840 \times 360$  cells at  $t = 5$ .

Define  $C_4 = \frac{1}{c_0} \left( \frac{1}{\gamma^{(2)-1}} - \frac{1}{\gamma^{(1)-1}} \right)$  and  $C_5 = \frac{1}{c_0(1-\gamma^{(2)})}$ , Eq. (B.8) can be written as

$$\begin{aligned} \bar{Y}_i^{n+1} = \bar{Y}_i^n - \frac{\Delta t}{\Delta x} \left( \nabla \mathbb{F}_Y^{k,\text{NOK}} + U_0 \left( 1 - e^{-\frac{1}{c_1}} \right) \sum_{l=1}^r \frac{\Delta t^l}{(l+1)!} \frac{\partial^l}{\partial t^l} \nabla Y^{e,\text{NOK}} \right) \\ + \left( C_4 \bar{Y}_i^{n+1} + C_5 \right) \left( \bar{p}_i^{n+1} - p_0 \right). \end{aligned} \tag{B.9}$$

Substituting Eq. (23) into Eq. (B.9) results in  $\bar{p}_i^{n+1} = p_0$ . Consequently, Eq. (18) is satisfied by MEHGKS. Based on a similar derivation, we can also prove that Eq. (18) is satisfied by MEHGKS-IS.

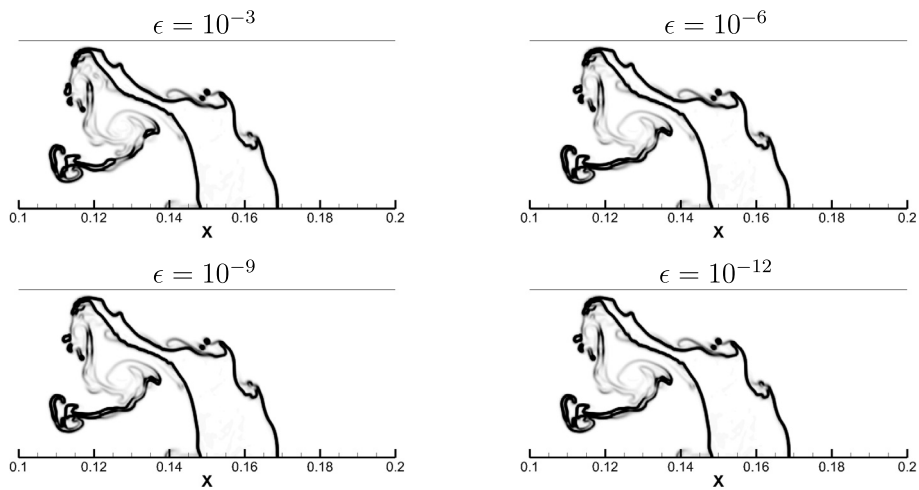


Fig. C.19. The schlieren-type images of  $\rho$  of the shock-bubble interaction problem (Section 4.10) with  $1780 \times 178$  cells at  $t = 1020 \times 10^{-6}$  (from top to bottom).

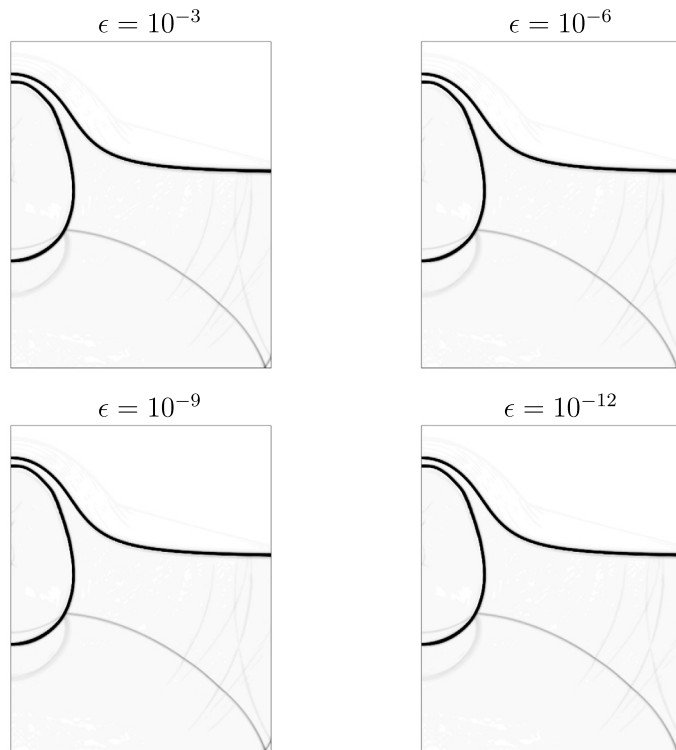


Fig. C.20. The schlieren-type images of  $\rho$  of the underwater explosion problem (Section 4.12) with  $400 \times 500$  cells at  $t = 1.2 \times 10^{-3}$ .

### Appendix C. The sensitivity of numerical results to $\epsilon$

$\epsilon$  is a small value used to identify a material interface. In this section, the results of several cases are given as an example to demonstrate their sensitivity to  $\epsilon$ , by using different values of  $\epsilon$  from  $10^{-3}$  to  $10^{-12}$ . The tests are conducted under the same conditions as the previous cases in Section 4, except for the value of  $\epsilon$ . The comparisons demonstrate that the numerical results are not sensitive to  $\epsilon$  in this range. See Figs. C.12–C.20.

### References

[1] R. Abgrall, How to prevent pressure oscillations in multicomponent flow calculation: a quasi conservative approach, J. Comput. Phys. 125 (1996) 150–160.

- [2] R. Abgrall, Residual distribution schemes: current status and future trends, *Comput. Fluids* 35 (2006) 641–669.
- [3] M.B. Artzi, J. Falcovitz, A second-order Godunov-type scheme for compressible fluid dynamics, *J. Comput. Phys.* 55 (1984) 1–32.
- [4] N. Ashgriz, J.Y. Poo, FLAIR: flux line-segment model for advection and interface reconstruction, *J. Comput. Phys.* 93 (1991) 449–468.
- [5] E. Aulisa, S. Manservigi, R. Scardovelli, S. Zaleski, A geometrical area-preserving volume-of-fluid advection method, *J. Comput. Phys.* 192 (2003) 355–364.
- [6] M. Ben-Artzi, J.Q. Li, G. Warnecke, A direct Eulerian GRP scheme for compressible fluid flows, *J. Comput. Phys.* 218 (2006) 19–43.
- [7] A. Cervone, S. Manservigi, R. Scardovelli, S. Zaleski, A geometrical predictor–corrector advection scheme and its application to the volume fraction function, *J. Comput. Phys.* 228 (2009) 406–419.
- [8] J. Chen, F. Zhang, T.G. Liu, A discontinuous Galerkin method for the simulation of compressible gas-gas and gas-water two-medium flows, *J. Comput. Phys.* 403 (2020) 109059.
- [9] Y.B. Chen, S. Jiang, Modified kinetic flux vector splitting schemes for compressible flows, *J. Comput. Phys.* 228 (2009) 3582–3604.
- [10] Y.B. Chen, S. Jiang, A non-oscillatory kinetic scheme for multi-component flows with the equation of state for a stiffened gas, *J. Comput. Math.* (2011) 661–683.
- [11] A. Chiapolino, P. Boivin, R. Saurel, A simple phase transition relaxation solver for liquid-vapor flows, *Int. J. Numer. Methods Fluids* 83 (2016) 583–605.
- [12] B. Cockburn, C.W. Shu, The Runge–Kutta discontinuous Galerkin method for conservation laws V: multidimensional systems, *J. Comput. Phys.* 141 (1998) 199–224.
- [13] X. Deng, S. Inaba, B. Xie, K.M. Shyue, F. Xiao, High fidelity discontinuity-resolving reconstruction for compressible multiphase flows with moving interfaces, *J. Comput. Phys.* 371 (2018) 945–966.
- [14] O. Desjardins, V. Moureau, H. Pitsch, An accurate conservative level set/ghost fluid method for simulating turbulent atomization, *J. Comput. Phys.* 227 (2008) 8395–8416.
- [15] M. Dumbser, O. Zanotti, A. Hidalgo, D.S. Balsara, ADER-WENO finite volume schemes with space-time adaptive mesh refinement, *J. Comput. Phys.* 248 (2013) 257–286.
- [16] M. Dumbser, O. Zanotti, R. Loubère, S. Diot, A posteriori subcell limiting of the discontinuous Galerkin finite element method for hyperbolic conservation laws, *J. Comput. Phys.* 278 (2014) 47–75.
- [17] R.P. Fedkiw, T. Aslam, B. Merriman, S. Osher, A non-oscillatory Eulerian approach to interfaces in multimaterial flows (the ghost fluid method), *J. Comput. Phys.* 152 (1999) 457–492.
- [18] E. Franquet, V. Perrier, Runger–Kutta discontinuous Galerkin method for interface flows with a maximum preserving limiter, *Comput. Fluids* 65 (2012) 2–7.
- [19] J. Grove, R. Menikoff, The anomalous reflection of a shock wave at a material interface, *J. Fluid Mech.* 219 (1990) 313–336.
- [20] J.F. Haas, B. Sturtevant, Interaction of weak shock waves with cylindrical and spherical gas inhomogeneities, *J. Fluid Mech.* 181 (1987) 41–76.
- [21] A. Harten, B. Engquist, S. Osher, S.R. Chakravarthy, Uniformly high order accurate essentially non-oscillatory schemes III, in: *Upwind and High-Resolution Schemes*, Springer, 1987, pp. 218–290.
- [22] Z.W. He, Y.C. Ruan, Y.Q. Yu, B.L. Tian, F. Xiao, Self-adjusting steepness-based schemes that preserve discontinuous structures in compressible flows, *J. Comput. Phys.* 463 (2022) 111268.
- [23] Z.W. He, B.L. Tian, Y.S. Zhang, F.J. Gao, Characteristic-based and interface-sharpening algorithm for high-order simulations of immiscible compressible multi-material flows, *J. Comput. Phys.* 333 (2017) 247–268.
- [24] M.T. Henry, S. Varadan, E. Johnsen, A new limiting procedure for discontinuous Galerkin methods applied to compressible multiphase flows with shocks and interfaces, *J. Comput. Phys.* 280 (2015) 489–509.
- [25] J. Hernández, J. López, P. Gómez, C. Zanzi, F. Faura, A new volume of fluid method in three dimensions—Part I: Multidimensional advection method with face-matched flux polyhedra, *Int. J. Numer. Methods Fluids* 58 (2010) 897–921.
- [26] X. Ji, F.X. Zhao, W. Shyy, K. Xu, A family of high-order gas-kinetic schemes and its comparison with Riemann solver based high-order methods, *J. Comput. Phys.* 356 (2018) 150–173.
- [27] G.S. Jiang, C.W. Shu, Efficient implementation of weighted ENO schemes, *J. Comput. Phys.* 126 (1996) 202–228.
- [28] E. Johnsen, T. Colonius, Implementation of WENO schemes in compressible multicomponent flow problems, *J. Comput. Phys.* 219 (2006) 715–732.
- [29] S. Kokh, F. Lagoutiere, An anti-diffusive numerical scheme for the simulation of interfaces between compressible fluids by means of a five-equation model, *J. Comput. Phys.* 229 (2010) 2773–2809.
- [30] J.Q. Li, Z.F. Du, A two-stage fourth order time-accurate discretization for Lax–Wendroff type flow solvers I. Hyperbolic conservation laws, *J. Sci. Comput.* 38 (2016) A3046–A3069.
- [31] Q.B. Li, A gas-kinetic Riemann solver for stiffened gas interface and its application in multimaterial flows, *Commun. Comput. Phys.* 25 (2019) 416–447.
- [32] Q.B. Li, An improved gas-kinetic scheme for multimaterial flows, *Commun. Comput. Phys.* 27 (2020) 145–166.
- [33] Q.B. Li, K. Xu, S. Fu, A high-order gas-kinetic Navier–Stokes flow solver, *J. Comput. Phys.* 229 (2010) 6715–6731.
- [34] S.Y. Li, Y.B. Chen, S. Jiang, An efficient high-order gas-kinetic scheme (I): Euler equations, *J. Comput. Phys.* 415 (2020) 109488.
- [35] S.Y. Li, D.M. Luo, J.X. Qiu, Y.B. Chen, A compact and efficient high-order gas-kinetic scheme, *J. Comput. Phys.* 447 (2021) 110661.
- [36] Y.S. Lian, K. Xu, A gas-kinetic scheme for multimaterial flows and its application in chemical reactions, *J. Comput. Phys.* 163 (2000) 349–375.
- [37] N. Liu, H.Z. Tang, A high-order accurate gas-kinetic scheme for one and two-dimensional flow simulation, *Commun. Comput. Phys.* 15 (2014) 911–943.
- [38] N. Liu, X.H. Xu, Y.B. Chen, High-order spectral volume scheme for multi-component flows using non-oscillatory kinetic flux, *Comput. Fluids* 152 (2017) 120–133.
- [39] D.M. Luo, S.Y. Li, W.Z. Huang, J.X. Qiu, Y.B. Chen, A quasi-conservative discontinuous Galerkin method for multi-component flows using the non-oscillatory kinetic flux II: ALE framework, *J. Sci. Comput.* 90 (2022) 1–35.
- [40] D.M. Luo, J.X. Qiu, J. Zhu, Y.B. Chen, A quasi-conservative discontinuous Galerkin method for multi-component flows using the non-oscillatory kinetic flux, *J. Sci. Comput.* 87 (2021) 1–32.
- [41] J. Luo, K. Xu, A high-order multidimensional gas-kinetic scheme for hydrodynamic equations, *Sci. China, Technol. Sci.* 56 (2013) 2370–2384.
- [42] J. Luo, L.J. Xuan, K. Xu, Comparison of fifth-order WENO scheme and finite volume WENO-gas-kinetic scheme for inviscid and viscous flow simulation, *Commun. Comput. Phys.* 14 (2013) 599–620.
- [43] J. von Neumann, R.D. Richtmyer, A method for the numerical calculation of hydrodynamic shocks, *J. Appl. Phys.* 21 (1950) 232.
- [44] G.X. Ni, W.H. Sun, A DGBGK scheme for compressible multi-fluids, *Int. J. Numer. Methods Fluids* 66 (2011) 760–777.
- [45] W.F. Noh, P. Woodward, SLIC (Simple Line Surface Calculation), *Lecture Notes in Physics*, vol. 59, Springer, 1976.
- [46] E. Olsson, G. Kreiss, S. Zehedi, A conservative level set method for two phase flow II, *J. Comput. Phys.* 225 (2007) 785–807.
- [47] L. Pan, J.X. Cheng, S.H. Wang, K. Xu, A two-stage fourth-order gas-kinetic scheme for compressible multicomponent flows, *Commun. Comput. Phys.* 22 (2017) 1123–1149.
- [48] L. Pan, K. Xu, Q.B. Li, J.Q. Li, An efficient and accurate two-stage fourth-order gas-kinetic scheme for the Euler and Navier–Stokes equations, *J. Comput. Phys.* 326 (2016) 197–221.
- [49] J.E. Pilliod, E.G. Puckett, Second-order accurate volume-of-fluid algorithms for tracking material interfaces, *J. Comput. Phys.* 199 (2004) 465–502.
- [50] A. Rehman, S. Qamar, High order finite-volume WENO scheme for five-equation model of compressible two-fluid flow, *Comput. Math. Appl.* 76 (2018) 2648–2664.

- [51] W.J. Rider, D.B. Kothe, Reconstructing volume tracking, *J. Comput. Phys.* 141 (1999) 112–152.
- [52] M.R. Saleem, I.A.S. Qamar, Application of discontinuous Galerkin method for solving a compressible five-equation two-phase flow model, *Results Phys.* 8 (2018) 379–390.
- [53] R. Saurel, C. Pantano, Diffuse-interface capturing methods for compressible two-phase flows, *Annu. Rev. Fluid Mech.* 50 (2018) 105–130.
- [54] C. Shen, *Rarefied Gas Dynamics: Fundamentals, Simulations and Micro Flows*, Springer Science & Business Media, 2006.
- [55] C.W. Shu, Essentially non-oscillatory and weighted essentially non-oscillatory schemes for hyperbolic conservation laws, in: *Advanced Numerical Approximation of Nonlinear Hyperbolic Equations*, Springer, 1998, pp. 325–432.
- [56] K.M. Shyue, An efficient shock-capturing algorithm for compressible multicomponent problems, *J. Comput. Phys.* 142 (1998) 208–242.
- [57] K.M. Shyue, A fluid-mixture type algorithm for compressible multicomponent flow with van der Waals equation of state, *J. Comput. Phys.* 156 (1999) 43–88.
- [58] K.M. Shyue, A wave-propagation based volume tracking method for compressible multicomponent flow in two space dimensions, *J. Comput. Phys.* 215 (2006) 219–244.
- [59] K.M. Shyue, F. Xiao, An Eulerian interface sharpening algorithm for compressible two-phase flow: the algebraic THINC approach, *J. Comput. Phys.* 268 (2014) 326–354.
- [60] K.K. So, X.Y. Hu, N.A. Adams, Anti-diffusion interface sharpening technique for two-phase compressible flow simulations, *J. Comput. Phys.* 231 (2012) 4304–4323.
- [61] Z.Y. Sun, S. Inaba, F. Xiao, Boundary Variation Diminishing (BVD) reconstruction: a new approach to improve Godunov scheme, *J. Comput. Phys.* 322 (2016) 309–325.
- [62] H. Terashima, G. Tryggvason, A front-tracking/ghost-fluid method for fluid interfaces in compressible flows, *J. Comput. Phys.* 228 (2009) 4012–4037.
- [63] V.A. Titarev, E.F. Toro, ADER: arbitrary high order Godunov approach, *J. Sci. Comput.* 17 (2002) 609–618.
- [64] A. Tiwari, J.B. Freund, C. Pantano, A diffuse interface model with immiscibility preservation, *J. Comput. Phys.* 252 (2013) 290–309.
- [65] E.F. Toro, R.C. Millington, L. Nejad, Towards very high order Godunov schemes, in: *Godunov Methods*, Springer, 2001, pp. 907–940.
- [66] F. Xiao, S. Li, C. Chen, Revisit to the THINC scheme: a simple algebraic VOF algorithm, *J. Comput. Phys.* 230 (2011) 7086–7092.
- [67] K. Xu, BGK-based scheme for multicomponent flow calculations, *J. Comput. Phys.* 134 (1997) 122–133.
- [68] K. Xu, *Gas-kinetic schemes for unsteady compressible flow simulations*, in: *Computational Fluid Dynamics*, in: *Annual Lecture Series*, vol. 29, Rhode-Saint-Genese, Belgium, 1998.
- [69] K. Xu, A gas-kinetic BGK scheme for the Navier-Stokes equations and its connection with artificial dissipation and Godunov method, *J. Comput. Phys.* 171 (2001) 289–335.
- [70] C. Zhang, I. Menshov, Eulerian model for simulating multi-fluid flows with an arbitrary number of immiscible compressible components, *J. Sci. Comput.* 83 (2020) 1–33.
- [71] D. Zhang, C.B. Jiang, D.F. Liang, Z.B. Chen, Y. Yang, Y. Shi, A refined volume-of-fluid algorithm for capturing sharp fluid interfaces on arbitrary meshes, *J. Comput. Phys.* 229 (2010) 6715–6731.
- [72] X.X. Zhang, C.W. Shu, Maximum-principle-satisfying and positivity-preserving high-order schemes for conservation laws: survey and new developments, *Proc. R. Soc. A, Math. Phys. Eng. Sci.* 467 (2011) 2752–2776.